Wall Position and Thickness Estimation from Sequences of Echocardiographic Images[1]

José M. B. Dias, *Member, IEEE,* and José M. N. Leitão
Instituto de Telecomunicações and
Departamento de Engenharia Electrotécnica e de Computadores,
Instituto Superior Técnico, Lisboa, PORTUGAL

Fax: 351.1.8418472 Email:edias@beta.ist.utl.pt

Abstract

This paper presents a new method for endocardial (inner) and epicardial (outer) contour estimation from sequences of echocardiographic images. The framework herein introduced is fine-tuned for parasternal short axis views at the papillary muscle level. The underlying model is probabilistic; it captures the relevant features of the image generation physical mechanisms and of the heart morphology. Contour sequences are assumed two-dimensional noncausal first order Markov random processes; each variable has a spatial index and a temporal index. The image pixels are modelled as Rayleigh distributed random variables with means depending on their positions (inside endocardium, between endocardium and pericardium, or outside pericardium). The complete probabilistic model is built under the Bayesian framework. As estimation criterion the *maximum a posteriori* (MAP) is adopted. To solve the optimization problem one is led to (joint estimation of contours and distributions' parameters), we introduce an algorithm herein named *iterative multigrid dynamic programming* (IMDP). It is a fully data driven scheme with no ad-hoc parameters. The method is implemented on an ordinary workstation, leading to computation times compatible with operational use. Experiments with simulated and real images are presented.

Key words: Echocardiography, Contour Estimation, Bayesian, Dynamic Programming.

[1] Refererence [1] is a short version of this work.

Two-dimensional echocardiography, when compared with other imaging techniques, exhibits attractive characteristics such as absence of an invasive agent, low cost, portability, real time processing, and direct three-dimensional acquisition (tomographic slices). These attributes justify the wide use of this image modality in the assessment of left ventricular function [2], [3], [4], [5].

Feature extraction from echocardiographic data is of major importance for quantitative analysis of the heart function [5], [6]. Examples of such features are: ventricular contours, volume of chambers, ejection fraction, thickness of myocardium, ventricular mass, and three-dimensional reconstruction/modeling throughout the cardiac cycle. Partial or total automation of this task, leading to reliable, objective, and reproducible analysis, is strongly desirable.

An echocardiographic expert is readily able to identify and retrieve information from video images or even from M-mode data. This is so, not only due to the ability of the human eye to integrate information, but also due to the inherent three-dimensional acquisition and real time characteristics of echocardiography. However, any automatic processing is hampered by the poor quality of echocardiographic images. Main degradation mechanisms include [7], [8], [9], [10]:

1. **Sidelobes and grating lobes:** the dynamic range of detected echoes is about 115 dB. With such a huge range, a low sidelobe level is crucial. Acoustic phased array transducers have had great improvements since their first days. For example, the sidelobes level of a modern transducer can be as low as -60 dB [9]; nevertheless, some weak echoes can still be masked by stronger echoes not coming from the point being imaged.

2. **Blur:** the dynamic focusing technique maintains the received wave focused. However, the transmitted pulse can only be focused for a fixed point (typically half of maximum range); this originates images having stronger blur near the transducer and near the maximum range than at middle range.

3. **Acquisition on polar coordinates:** data acquisition on polar coordinates leads to a nonuniform inter-sampling space. Due to the sparseness of samples, for large ranges, some kind of interpolation is necessary. This confers a nonhomogeneous characteristic to the echocardiographic image.

4. **Poor contrast:** little contrast between blood and myocardium (due to the similar acoustic characteristics) makes the determination of the endocardium border difficult. This is also true in some parts of the pericardium where there is no contrast at all.

5. **Artifacts:** artifacts like papillary muscles, valves, and chordae should be previously detected not to interfere with posterior processing. This task can be hard to attain since artifacts themselves

6. **Speckle noise:** speckle noise is the major difficulty concerning echocardiographic image processing; it is inherent to coherent illumination and Rayleigh scattering caused by tissue microstructures. The echo from a resolution volume, confined by the lateral and the range transducer resolutions, is the sum of all echoes from the scatterers (tissue cells, tissue fibers, and small internal structural details) in that resolution volume. Each particular configuration of scatterers produces constructive or destructive interference of the backscattered echoes. Assuming that, in each element of volume, the number of scatterers is large and their positions are randomly distributed within the wave length, then the echo amplitude is characterized by a Rayleigh random variable [11]. Under these conditions, the signal to noise ratio (SNR) associated with an image pixel, defined as its mean value divided by its standard deviation, amounts to 1.91 (see [7]). The high-contrast high-spatial-frequency noise, masking acoustic images, is a consequence of this poor SNR.

A. Previous work on contour estimation

Contour estimation (from a frame or from a sequence of frames) has been the main objective of most works on semi-automatic or automatic feature extraction from echocardiographic data [10], [12], [13], [14], [15], [16], [17]; this is a consequence of the huge amount of structural information carried by boundaries. Moreover, contours are the base of most quantitative procedures.

The many noisy effects plaguing two-dimensional echocardiographic data (the most important being the speckle noise) make conventional techniques based on edge enhancement (e.g., gradient, compass, threshold, and Laplace operators) inappropriate to contour estimation. An example illustrating the inadequacy of this operators in echocardiographic data is given in [10]: a 4-chamber image is processed by a Sobel edge detector with an interactively defined optimal thresholding level; as a result "... no continuous contour can be drawn and therefore edges of myocardial wall are ill-defined." A similar conclusion can also be found in [12]. More elaborated approaches such as the Canny [18] step edge detectors or algorithms emerging from using *compound Gauss-Markov random fields* [19], [20], [21], [22] are not suited to echocardiographic data, as well, since they are not designed to cope with speckle noise.

In face of this, different *ad hoc* contour estimation algorithms have been proposed. Adam *et al.* [10] present a scheme to semiautomatically track ventricular endocardial and epicardial borders. Their approach includes nonlinear Median filtering (size 9×9) of whole images, debiasing of gray levels, and location-dependent contrast stretching. The algorithms tracks the movement of a small number of predetermined points, which are manually defined on the two myocardial borders. Chu *et al.* [12] proposed a three steps algorithm (edge detection, radial search for initial

epicardial boundaries. The edge detector includes a by a 41×41 Gaussian filter followed by a Laplacian operator. Joseph *et al.* [13] applied mathematical morphology to semiautomatically detecting the left ventricular endocardial border. Temporal smoothing (10 frames) is implemented. Friedland *et al.* [14], proposed a fully automatic ventricular boundary detection from sequential images using simulated annealing. Before contour estimation, images undergo low pass filtering to (7×7 FIR) followed by a $4:1 \times 4:1$ decimation. Unser *et al.* [15] introduced a method for automated extraction of myocardial borders in M-mode echocardiograms using suitable matched filters. Steen *et al.* [17] developed a boundary detection scheme based on anisotropic diffusion. Anisotropic diffusion implements low pass filtering within homogeneous regions and preserves or enhances the region boundaries.

We would like to call the attention to the smoothing (typically the first step) implemented in the above referred works. A common argument justifying the spatial smoothing is that the relevant spatial information remains almost unchanged, as it resides at low frequencies. Since the speckle sizes are of the order of the spatial resolution of the imaging system, this argument is doubtful [23].

B. Proposed approach to contour estimation

The present work aims at endocardial and epicardial contour estimation in the parasternal short axis view. Since both contours are estimated, the thickness of the myocardium is a spin-off result. The following aspects play a crucial role in the proposed approach:

1. **Image characterization:** given a tissue configuration, the respective image is assumed pixelwise independent; each pixel is Rayleigh distributed with its parameter being a function of the correspondent acoustic characteristics.

2. **Heart morphology:** the image formed by the parameters (a parameter per pixel) has a structure that should be taken into account. For example, if parameters are scanned along a path from inside to outside the heart, their value are likely to exhibit a rectangular type shape.

3. **Contour model:** contour sequences are assumed samples of two-dimensional noncausal first order Markov random processes: each random variable has a spatial index and a temporal index. Therefore, in each image, contours are represented in an one-dimensional coordinate system.

4. **Bayesian formulation and MAP criterion:** by using the Bayesian formulation, the *a posteriori* probability, which includes the *a priori* probability of contours, is built. The MAP criterion is then applied to estimate the contours.

one is led to (joint estimation of contours and distributions' parameters), we conceive an algorithm herein named *iterative multigrid dynamic programming* (IMDP). According to its name it embodies *iterative*, *dynamic progamming* and *multigrid* concepts.

The developed approach is new in the sense that we build a probabilistic model based on the relevant features of the image generation physical mechanisms and of the heart morphology (items 1,2, and 3); underlying the contour estimates is a new edge detector (emerging from the proposed framework); it is a *long range* operator (matched filter type) which is quite different from the local edge detectors used in [10], [12], [13], [14], [16].

As mentioned before, the IMDP algorithm encompasses iterative, dynamic programming, and multigrid concepts. Dynamic programming has already been used in other image modalities (see [24], [25], [26], [27], [28]) as a tool to estimate contours. However, the scenario herein considered is different; namely, it includes two contours (inner and outer) and temporal dimension.

The paper organization is now briefly presented. Section II introduces notation, the coordinate system, and the adopted contour spatial prior. Section III develops the image generation mechanism. In section IV, a one-dimensional causal first-order Markov random process is introduced to describe the temporal sequence of contours; a probabilistic model including temporal and spatial dimensions is then presented. Section V describes the IMDP algorithm. Section VI presents results from simulated and real data.

II. Probabilistic Model of Endocardial and Epicardial Contours

Fig. 1 schematizes the adopted (one-dimensional) polar coordinate system. The endocardial contour is represented by the M-dimensional vector $\mathbf{r}^1 = [r_0^1, \ldots, r_{M-1}^1]^T$. The epicardial contour $\mathbf{r}^2$ is defined in the same way, replacing index 1 by 2. Both vectors are collected in $\mathbf{r} = [\mathbf{r}^1, \mathbf{r}^2]$. We also define $\mathbf{r}_i = [r_i^1, r_i^2]$, a vector holding both contour positions at the i-th scan-line. The angle of each scan-line is $\theta_i = (2\pi i)/M$, with $i = 0, \ldots, M-1$.

Since we are dealing with digital images, defined on a rectangular lattice, each coordinate r_i^k (with $k \in \{1, 2\}$) can only take values in the discrete set Λ_i^k which has N_i elements:

$$\Lambda_i^1 = \Lambda_i^2 = \{d_i(1), d_i(2), \cdots, d_i(N_i)\}, \quad d_i \in \Re^+. \tag{1}$$

Notice that for each $r_i^1 \in \Lambda_i^1$ there is one and only one $k_i^1 \in \{1, \cdots, N_i\}$ such that $r_i^1 = d_i(k_i^1)$. Along the text, we sometimes refer to the integers k_i^1 and/or k_i^2, instead of contour positions r_i^1 and/or r_i^2. For the same reason, the entities $\mathbf{k}^1 = [k_0^1, \ldots, k_{M-1}^1]^T$, $\mathbf{k}^2 = [k_0^2, \ldots, k_{M-1}^2]^T$, $\mathbf{k} = [\mathbf{k}^1, \mathbf{k}^2]$, and $\mathbf{k}_i = [k_i^1, k_i^2]$ are also introduced. It should be stressed that the mapping from the r-entities ($\mathbf{r}$, $\mathbf{r}^1$, $\mathbf{r}^2$, $\mathbf{r}_i$) to the k-entities ($\mathbf{k}$, $\mathbf{k}^1$, $\mathbf{k}^2$, $\mathbf{k}_i$) is one-to-one, thus, being equivalent to

$\mathbf{\Lambda} = \prod_{i=0,k=1}^{i=M-1,k=2} \Lambda_i^k$ is introduced to be used in due course.

The only human intervention in the boundary extraction process is the selection of a point inside the inner contour. If this point is selected above the latitude defined by the papillary muscles, the polar coordinate system adopted is able to describe most of the contours in the short axis view. Moreover, if this image is acquired at the end-systole (or in its neighborhood) the same polar coordinate system can be used for the whole sequence. There are, however, some pathological contours for which the choice of this point is critical or even impossible (the contour cannot be represented in polar coordinates). These situations are not considered in this work.

The polar (one-dimensional) coordinate system has been frequently used in contour estimation problems (e.g., [12], [14], [25], [29]). Other one-dimensional coordinate systems have also been adopted; relevant examples are reported in [30] and [31], for endocardial contour estimation from angiographic images, and [32] for coronary artery estimation from angiograms.

Two-dimensional coordinate systems (as proposed in [27] and [33]), when compared with one-dimensional coordinate systems, are able to describe a wider class of contours. On the other hand, one-dimensional coordinate systems are easier to deal with, from the computational and analytical standpoints. One-dimensional coordinate systems can be viewed as two-dimensional ones with constraints. This is not always a disadvantage: for example, in adopting a polar coordinate system we are solely interested in contours defining a function in the (θ, r) plane. In a certain sense, this is a form of inserting *a priori* information about contours.

A. Prior contour model

Heart contours are continuous: given vectors $\mathbf{r}_{i-1}$ and $\mathbf{r}_{i+1}$, vector $\mathbf{r}_i$ must be close. In the probabilistic framework, this property is modelled by assuming that contours in a frame are one-dimensional noncausal first order Markov random fields (to our knowledge, describing echographic contours with Markovian models was firstly proposed in [14]). This property is expressed as

$$P(\mathbf{r}_i|\mathbf{r}_j, j \neq i) = P(\mathbf{r}_i|\mathbf{r}_j, j \in \mathcal{G}_i), \tag{2}$$

for $i \in S = \{0, \ldots, M-1\}$. Sets $\mathcal{G}_i = \{i-1, i+1\}$ and $\mathcal{G} = \{\mathcal{G}_i, i \in S\}$ are termed the *neighborhood* of i and the *neighborhood system*, respectively [34], [35]. Given the cyclic nature of contours, we impose $\mathcal{G}_0 = \{M-1, 1\}$ and $\mathcal{G}_{M-1} = \{M-2, 0\}$ (the so-called *periodic or cyclic* boundary).

The Hammersley-Clifford result, proved in [35], assures that if $P(\mathbf{r}) > 0$, $\forall \mathbf{r} \in \mathbf{\Lambda}$, the *joint* probability $P(\mathbf{r})$ is *uniquely* determined by the *conditional probabilities* (2). The concept of *clique* plays a central role in this result. A clique C is a set of either a single element $j \in S$, or of mutually neighbor sites. The set of cliques $\mathcal{C}$ associated to the neighborhood system $\mathcal{G}$ is

as

$$p(\mathbf{r}) = \frac{1}{Z} \exp\left\{ - \sum_{C \in \mathcal{C}} V_C(\mathbf{r}) \right\}, \tag{3}$$

where Z is a normalizing constant and $V_C(\mathbf{r}) = V_C(\mathbf{r}_i, i \in C)$ are functions termed *clique potentials*. The conditional probabilities (2) are derived from (3) by applying the Bayes law [34], yielding

$$P(\mathbf{r}_i | \mathbf{r}_j, j \in \mathcal{G}_i) = \frac{1}{Z_i} \exp\left\{ - \sum_{C : i \in C} V_C(\mathbf{r}) \right\}, \tag{4}$$

with Z_i denoting a normalizing constant.

Probability $P(\mathbf{r})$ is to be tailored according to prior knowledge about the contours by specifying the clique potentials $V_C(\mathbf{r})$.

III. Image Generation Model

As referred in Section I, the echo amplitude generated by tissues is Rayleigh distributed. This assumption has been experimentally and theoretically confirmed [7], [36], [37].

The echo signal, even after the *time gain compensation*[2], exhibits, roughly, 55 dB of dynamic range [38]. On the other hand, our visual system is only able to distinguish about 200 levels, i.e. 23 dB. For this reason, the receiver usually includes nonlinear signal compression. This nonlinearity is known for each equipment and should be taken into account, since it changes the Rayleigh distribution of the pixels at the acoustic transducer output.

The data used in this work was acquired by a system using as compressing nonlinearity a blend between a linear component and a logarithmic component. The logarithmic component was set to almost zero. In face of this, we still assume that the pixel amplitudes are Rayleigh distributed.

We take as hypothesis that pixels in a frame, conditioned on their mean values, are independent. It is the so-called *conditional independence* property [34]. This is a correct assumption if the *resolution volumes* contributing to different pixels are disjoint. Resolution volume depends on the lateral transducer resolution and on the pulse length. Despite the great resolution of phased array transducers, the independence hypothesis is hardly verified for every image pixel. This is mainly due to the nonhomogeneous nature of echographic data: for large ranges the process of converting polar coordinates into cartesian coordinates introduces correlation. Nonetheless, we still use the independence hypothesis since it is true for a large part of image pixels and leads to good contour estimates with an acceptable model complexity.

Let the pair of indexes (i, j), with $j = 1, \ldots, N_i$ and $i = 0, \ldots, M-1$, denote the j-th pixel along the i-th radial scan-line. The gray-level of pixel (i, j) is denoted by x_{ij}. If the inner contour

[2]Correction of the geometric factor $1/(range)$.

same applies to the outer contour.

Define $\sigma_{ij} \equiv \sqrt{\frac{2}{\pi}}\, E[x_{ij}]$ as a quantity called *reflectivity*. We assume that the reflectivity σ_{ij}, along a scan-line, is piecewise constant:

$$\sigma_{ij} = \begin{cases} \sigma_i^0 & 1 \leq j \leq k_i^1 \\ \sigma_i^1 & k_i^1 < j \leq k_i^2 \\ \sigma_i^2 & k_i^2 < j \leq N_i. \end{cases} \tag{5}$$

Hypothesis (5) is equivalent to stating that reflectivity is constant inside each type of tissue (blood, myocardium, and outside heart) along a scan-line.

We are now in position to come out with the probability $P(\mathbf{I}|\mathbf{r})$. The conditional independence implies that

$$P(\mathbf{I}|\mathbf{r}) = \prod_{i=0}^{i=M-1} P(\mathbf{I}_i|\mathbf{r}_i), \tag{6}$$

where $\mathbf{I}_i = [x_{i1}, \ldots, x_{iN_i}]^T$ contains the observed image gray-levels along the i-th scan-line. Using the Rayleigh distribution hypothesis, one obtains:

$$\begin{aligned} P(\mathbf{I}_i|\mathbf{r}_i, \boldsymbol{\sigma_i}) \;=\; & \prod_{j=1}^{k_i^1} \frac{x_{ij}}{(\sigma_i^0)^2} \exp\left[-\frac{1}{2}\left(\frac{x_{ij}}{\sigma_i^0}\right)^2\right] \\ & \prod_{j=k_i^1+1}^{k_i^2} \frac{x_{ij}}{(\sigma_i^1)^2} \exp\left[-\frac{1}{2}\left(\frac{x_{ij}}{\sigma_i^1}\right)^2\right] \\ & \prod_{j=k_i^2+1}^{N_i} \frac{x_{ij}}{(\sigma_i^2)^2} \exp\left[-\frac{1}{2}\left(\frac{x_{ij}}{\sigma_i^2}\right)^2\right], \end{aligned} \tag{7}$$

with $\boldsymbol{\sigma_i} = [\sigma_i^0, \sigma_i^1, \sigma_i^2]$.

Applying logarithm to (7) and after some simple manipulation, one is led to the *log-likelihood function* of a scan-line as

$$\begin{aligned} L(\mathbf{I}_i|\mathbf{r}_i, \boldsymbol{\sigma_i}) &= \ln P(\mathbf{I}_i|\mathbf{r}_i, \boldsymbol{\sigma_i}) \\ &= k_i^1 \ln\left(\frac{\sigma_i^1}{\sigma_i^0}\right)^2 + k_i^2 \ln\left(\frac{\sigma_i^2}{\sigma_i^1}\right)^2 - N_i \ln\left(\sigma_i^2\right)^2 - \frac{1}{2}\mathbf{I}_i^T[\mathbf{A}(\mathbf{r}_i, \boldsymbol{\sigma_i})]^{-1}\mathbf{I}_i + c^t, \end{aligned} \tag{8}$$

where $\mathbf{A}(\mathbf{r}_i, \boldsymbol{\sigma_i})$ is a diagonal matrix whose entries are the squared reflectivities according to (5).

Fig. 2 plots the echo along a radial line from the blood, inside the heart, towards the lungs. Roughly, it can be said that the endocardium is near $r = 45$ and the pericardium is near $r = 80$. Between $r = 0$ and $r = 44$ there is blood with reflectivity σ^0; between $r = 45$ and $r = 79$ there is myocardium with reflectivity σ^1; finally, for $r > 79$ there is lung tissue with reflectivity σ^2. The high value of σ^2 is caused by the lungs, and saturates the receiver between $r = 80$ and $r = 90$, approximately.

position r^1. The parameters $r^2 = 77$, $\sigma^0 = 14.6$, $\sigma^1 = 58.1$, $\sigma^2 = 161.5$, and $r^1 = 47$ maximize this log-likelihood function.

The observation model just presented has some similarities with the one proposed in [29]. In both models, the physical aspects of image generation yield probability $P(\mathbf{I}|\mathbf{r})$. However, the latter applies to X-ray angiographic image modality, where the underlying statistic model is quite different.

IV. The Complete Model

We are now in position to expand the posterior probability $P(\mathbf{r}|\mathbf{I}) \propto P(\mathbf{I}|\mathbf{r})P(\mathbf{r})$ in terms of the prior $P(\mathbf{r})$ and of the image generation model $P(\mathbf{I}|\mathbf{r})$. From equations (6) and (3), it follows that

$$\begin{aligned} \Psi(\mathbf{r}|\mathbf{I},\boldsymbol{\sigma}) &= \ln P(\mathbf{r}|\mathbf{I},\boldsymbol{\sigma}) \\ &= \sum_{i=0}^{i=M-1} L(\mathbf{I}_i|\mathbf{r}_i,\boldsymbol{\sigma}_i) - \sum_{C\in\mathcal{C}} V_C(\mathbf{r}) + c^t, \end{aligned} \tag{9}$$

with $\boldsymbol{\sigma} = [\boldsymbol{\sigma}^0, \boldsymbol{\sigma}^1, \boldsymbol{\sigma}^2]$ and $\boldsymbol{\sigma}^j = [\sigma_0^j, \cdots, \sigma_{M-1}^j]^T$, for $j = 1, 2, 3$. The MAP estimate is then

$$\widehat{\mathbf{r}}_{MAP} = \arg\max_{\mathbf{r}} \Psi(\mathbf{r}|\mathbf{I},\boldsymbol{\sigma}). \tag{10}$$

Define $\phi_i(\mathbf{r})$ as

$$\phi_i(\mathbf{r}) \equiv V_{\{i\}}(\mathbf{r}) + V_{\{i-1,i\}}(\mathbf{r}), \tag{11}$$

where $V_{\{i\}}(\mathbf{r})$ and $V_{\{i-1,i\}}(\mathbf{r})$ are the potentials of cliques $\{i\}$ and $\{i-1, i\}$, respectively. Function $\phi_i(\mathbf{r})$ is intended to model prior knowledge about the contour. In this work we consider the linear composition

$$\phi_i(\mathbf{r}) = \sum_{k=1}^{k=4} \phi_i^k(\mathbf{r}), \tag{12}$$

which includes:

1. A constraining term

$$\phi_i^1(\mathbf{r}) = \begin{cases} 0 & R_{min} < r_i^2 - r_i^1 < R_{max} \\ \infty & R_{min} \geq r_i^2 - r_i^1 \geq R_{max}, \end{cases} \tag{13}$$

which restricts the displacement between endocardial and epicardial borders to the interval (R_{min}, R_{max}). These limits were set to 10 and 100, respectively[3].

[3] All the distance measures are given in units of length. In the present setup 1 unit of length = 0.27 mm.

$$\phi_i^2(\mathbf{r}) = \alpha_1(r_i^1 - r_{i-1}^1)^2, \tag{14}$$

penalizing large steps on two consecutive radial border positions. The parameter α_1 is set to $\frac{10^2}{M^2}$ (this value was estimated from synthetic data).

3. A pericardial smoothness term

$$\phi_i^3(\mathbf{r}) = \alpha_2(r_i^2 - r_{i-1}^2)^2, \tag{15}$$

playing a role similar to ϕ^2. The parameter α_2 is set to $\frac{5\times10^2}{M^2}$ (again, this value was estimated from synthetic data). Notice that α_2 is five times greater than α_1. This makes sense since, in the short axis view, the pericardial contour, is expected to be much smoother than the endocardial contour.

4. An endocardium maximum volume term

$$\phi_i^4(\mathbf{r}) = \beta_1 \frac{1}{r_i^1}, \tag{16}$$

which pushes the estimated endocardial contour outowards allowing it to pass over artifacts inside the heart. However, in some cases the attraction strength originated by artifacts is so strong that the maximum volume element is not enough to solve the problem. Parameter β_1 is set to 1000.

A. Modeling image sequences

Typically, echographic systems output a 25 frames per second video signal. Considering a maximum tissue velocity of 30 mm/s, the maximum displacement between two consecutive frames is of 1.2 mm. This means that the structures being imaged in two consecutive frames are spatially very close. On the other hand, it is likely that a missed or unclear detail in a frame appears clearer displayed on a neighbor frame. A specialist explores this temporal information by looking at the temporal neighbors of a given frame. Likewise, we will include temporal information into our order aiming at better estimates.

Denote the n-th frame of a temporal sequence by $\mathbf{I}(n)$. Suppose that frames $\mathbf{I}(n-1)$ and $\mathbf{I}(n)$ are observed. Assuming the observation model presented in Section III, and applying the Bayes law, the joint probability of $\mathbf{r}(n)$, $\mathbf{r}(n-1)$, $\mathbf{I}(n-1)$ and $\mathbf{I}(n)$ can be expanded as

$$\begin{aligned} &P\big(\mathbf{r}(n), \mathbf{I}(n), \mathbf{r}(n-1), \mathbf{I}(n-1)\big) \\ &\quad = P\big(\mathbf{I}(n)|\mathbf{r}(n)\big)P\big(\mathbf{r}(n), \mathbf{r}(n-1), \mathbf{I}(n-1)\big) \\ &\quad = P\big(\mathbf{I}(n)|\mathbf{r}(n)\big)P\big(\mathbf{I}(n-1)|\mathbf{r}(n-1)\big)P\big(\mathbf{r}(n-1), \mathbf{r}(n)\big) \\ &\quad = P\big(\mathbf{I}(n)|\mathbf{r}(n)\big)P\big(\mathbf{I}(n-1)|\mathbf{r}(n-1)\big)P\big(\mathbf{r}(n-1)|\mathbf{r}(n)\big)P\big(\mathbf{r}(n)\big). \end{aligned} \tag{17}$$

$$\mathbf{r}(n) = \mathbf{r}(n-1) + \boldsymbol{\varepsilon}(n), \tag{18}$$

with $\boldsymbol{\varepsilon}(n)$ being a zero mean white Gaussian noise vector whose elements have variances $\sigma^2[\varepsilon_i]$. Roughly, hypothesis (18) states that contour $\mathbf{r}(n)$ lies within a cloud of size[4] 3σ around $\mathbf{r}(n-1)$. In fact, we should have assumed a mean $\mathbf{a}(n) \neq \mathbf{0}$ for vector $\boldsymbol{\varepsilon}(n)$, in order to prevent bias from happening. However, mean $\mathbf{a}(n)$, is not *a priori* known, and it would have to be estimated. This would introduce complexity in the model beyond a reasonable limit. On the other hand, our main intention in introducing the temporal dimension in the model is to define a region of high probability where to find $\mathbf{r}(n)$ given $\mathbf{r}(n-1)$. This prevents estimated borders from getting stuck on artifacts lying far from the true borders.

The maximum border displacement between two consecutive frames is rarely greater than 1 mm. Variance σ^2 was set to 1 mm^2. This value guarantees almost no bias, and, on the other hand, it confines consecutive borders to a relatively small uncertainty cloud.

The *a posteriori* objective function, including two consecutive frames, is given by

$$\begin{aligned}
&\Psi_n\big(\mathbf{r}(n), \mathbf{r}(n-1) | \boldsymbol{\sigma}(n), \boldsymbol{\sigma}(n-1)\big) \\
&\qquad = \ln P\big(\mathbf{r}(n), \mathbf{r}(n-1) | \mathbf{I}(n), \mathbf{I}(n-1), \boldsymbol{\sigma}(n), \boldsymbol{\sigma}(n-1)\big) \\
&\qquad = \sum_{t=n-1}^{n} \sum_{i=0}^{i=M-1} L\big(\mathbf{I}_i(t) | \mathbf{r}_i(t), \boldsymbol{\sigma}_i(t)\big) - \sum_{i=0}^{M-1} \sum_{k=1}^{5} \phi_i^k\big(\mathbf{r}(n), \mathbf{r}(n-1)\big) + c^t,
\end{aligned} \tag{19}$$

with $\phi_i^k\big(\mathbf{r}(n), \mathbf{r}(n-1)\big) = \phi_i^k\big(\mathbf{r}(n)\big)$ for $k = 1, \ldots, 4$, and

$$\phi_i^5\big(\mathbf{r}(n), \mathbf{r}(n-1)\big) = \frac{1}{2\sigma} \left\| \mathbf{r}_i(n) - \mathbf{r}_i(n-1) \right\|^2, \tag{20}$$

where $\|(\cdot)\|$ stands for Euclidian norm.

V. The Optimization Algorithm

A. Introduction

The MAP estimates of endocardial and epicardial borders are given by

$$\big(\widehat{\mathbf{r}}_{MAP}(n), \widehat{\mathbf{r}}_{MAP}(n-1)\big) = \arg \max_{\mathbf{r}(n), \mathbf{r}(n-1)} \Psi_n. \tag{21}$$

Objective function Ψ_n given by (19) is nonconvex and depends on $2M$ radii variables and $3M$ reflectivity parameters. Even assuming that the vector of parameters $\boldsymbol{\sigma}$ is known, an exhaustive search over the set $\boldsymbol{\Lambda}$ would lead to, approximately, $\prod_{i=1}^{2M} (N_i^2/2)$ evaluations of Ψ_n. With $M = 32$

[4]The set $A_i^k(n) = \{r_i^k(n) : |r_i^k(n) - r_i^k(n-1)| \leq 3\sigma\}$ has probability $P(A_i^k(n)) = 0.99$.

optimization algorithm should be looked for.

Simulated annealing, a stochastic relaxation technique [39], [34], was applied in [14]. The estimates provided by this technique might converge in probability (if a slow enough temperature schedule is chosen), but at the expense of an intolerable computational burden. *Coordinate descendent or gradient based methods* [40] do not yield good estimates, as well, since the objective function Ψ_n is highly nonconvex.

B. The adopted criterion

Reflectivity vectors $\boldsymbol{\sigma}(n)$ and $\boldsymbol{\sigma}(n-1)$ are unknown; within the Bayesian framework, we assume they are uniformly distributed. Like vector $\mathbf{r}(n)$ and $\mathbf{r}(n-1)$, they must also be estimated from Ψ_n:

$$\big(\widehat{\mathbf{r}}_{MAP}(n), \widehat{\mathbf{r}}_{MAP}(n-1), \widehat{\boldsymbol{\sigma}}_{MAP}(n), \widehat{\boldsymbol{\sigma}}_{MAP}(n-1)\big) \;=\; \arg \max_{\mathbf{r}(n),\mathbf{r}(n-1),\boldsymbol{\sigma}(n),\boldsymbol{\sigma}(n-1)} \Psi_n. \tag{22}$$

If the joint estimation of $\big(\mathbf{r}(n), \mathbf{r}(n-1)\big)$ is, by itself, extremely demanding, the joint estimation of $\big(\mathbf{r}(n), \mathbf{r}(n-1), \boldsymbol{\sigma}(n), \boldsymbol{\sigma}(n-1)\big)$ is unfeasible.

Let the observed sequence $\mathbf{I}(0), \ldots, \mathbf{I}(n)$ of images and the initial estimate $\widehat{\mathbf{r}}(0)$ be given. Consider the following recursive criterion:

$$\big(\widehat{\mathbf{r}}(n), \widehat{\boldsymbol{\sigma}}(n)\big) = \arg \max_{\mathbf{r},\boldsymbol{\sigma}} \Psi_n\big(\mathbf{r}, \widehat{\mathbf{r}}(n-1) | \boldsymbol{\sigma}, \widehat{\boldsymbol{\sigma}}(n-1)\big) \tag{23}$$

All solutions of (22) are also solutions of (23), however, the converse is not true. Thus, the criterion (23) is weaker than (22). Anyway, (23) is going to be applied, since the solutions it provides are very close to the ones provided by (22). In the case of $\sigma = \infty$ (absence of temporal cliques) both criteria would lead to the same set of solutions. Since a weak temporal energy was chosen, the solutions one is led to in both cases have to be close.

To achieve the solution according to criterion (23), we apply the following iterative scheme:

$$\widehat{\mathbf{r}}^{t+1}(n) \;=\; \arg \max_{\mathbf{r}} \Psi_n\big(\mathbf{r}, \widehat{\mathbf{r}}(n-1) | \widehat{\boldsymbol{\sigma}}^t(n), \widehat{\boldsymbol{\sigma}}(n-1)\big) \tag{24}$$

$$\widehat{\boldsymbol{\sigma}}^{t+1}(n) \;=\; \arg \max_{\boldsymbol{\sigma}} \Psi_n\big(\widehat{\mathbf{r}}^t(n), \widehat{\mathbf{r}}(n-1) | \boldsymbol{\sigma}, \widehat{\boldsymbol{\sigma}}(n-1)\big). \tag{25}$$

It is straightforward to show that the solutions of (23) are the only stationary points of (24)-(25).

Equation (25) is derived in a simple way from (8). One obtains

$$\widehat{\sigma}_i^{0t}(n) \;=\; \left[\frac{\mathbf{I}_i^T(n)\mathbf{D}_i^0(\widehat{\mathbf{r}}_i^t)\mathbf{I}_i(n)}{2k_i^{1t}}\right]^{\frac{1}{2}} \tag{26}$$

$$\widehat{\sigma}_i^{1t}(n) \;=\; \left[\frac{\mathbf{I}_i^T(n)\mathbf{D}_i^1(\widehat{\mathbf{r}}_i^t)\mathbf{I}_i(n)}{2(k_i^{2t} - k_i^{1t})}\right]^{\frac{1}{2}} \tag{27}$$

$$\widehat{\sigma}_i^{2t}(n) \;=\; \left[\frac{\mathbf{I}_i^T(n)\mathbf{D}_i^2(\widehat{\mathbf{r}}_i^t)\mathbf{I}_i(n)}{2(N_i - k_i^{2t})}\right]^{\frac{1}{2}}, \tag{28}$$

$1 \leq j \leq k_i^{1t}$ (notation X^{st} stands for the entity X^s at the t-th iteration). Matrices $\mathbf{D}_i^1$ and $\mathbf{D}_i^2$ are defined in the same way for $k_i^{1t} < j \leq k_i^{2t}$ and $k_i^{2t} < j \leq N_i$, respectively. Notice that estimates $\widehat{\sigma}_i^{0t}(n)$, $\widehat{\sigma}_i^{1t}(n)$, and $\widehat{\sigma}_i^{2t}(n)$ are nothing but sample second moments of x_{ij}.

Contrarily to the easiness of (25), each step of iteration (24) is very demanding since Ψ_n is a nonconvex function of $\mathbf{r}(n)$. A Bellman-Ford type [41] algorithm, herein termed iterative multigrid dynamic programming (IMDP) algorithm, is proposed to achieve the solution $\widehat{\mathbf{r}}(n)$.

C. The IMDP algorithm

Function Ψ_n in equation (24) is to be maximized with respect to $\mathbf{r}$. Let $\Psi_n(\mathbf{r}) = \Psi_n(\mathbf{r}^1, \mathbf{r}^2)$ denote Ψ_n, with $\mathbf{r}(n-1)$, $\boldsymbol{\sigma}(n)$, and $\boldsymbol{\sigma}(n-1)$ fixed.

Having in mind the definition of vectors $\mathbf{k}^1$ and $\mathbf{k}^2$, one can write

$$\Psi_n(\mathbf{r}^1, \mathbf{r}^2) = \sum_{i=0}^{i=M-1} a_i(k_{i-1}^1, k_i^1, k_{i-1}^2, k_i^2), \tag{29}$$

where

$$a_i(k_{i-1}^1, k_i^1, k_{i-1}^2, k_i^2) \;\; = \;\; L(\mathbf{I}_i(n)|\mathbf{r}_i(n), \boldsymbol{\sigma}_i(n)) - \sum_{k=1}^{5} \phi_i^k\big(\mathbf{r}(n), \mathbf{r}(n-1)\big). \tag{30}$$

For a while admit also $\mathbf{r}^2$ fixed. This is equivalent to assuming k_i^2 and k_{i-1}^2 fixed. In this case we denote the term $a_i(\cdot)$ in (30) as $a_i(k_{i-1}^1, k_i^1)$, and function $\Psi_n(\mathbf{r}^1, \mathbf{r}^2)$ as $\Psi_n(\mathbf{r}^1)$.

Maximization of $\Psi_n(\mathbf{r}^1)$ is equivalent to finding the high cost path on a directed graph with the set of nodes $\mathcal{N} = \{(i,k) | i = 0, \ldots, M-1,\ k = 1, \ldots, N_i\}$. The cost between node (i,n) and the node $(i-1, m)$, is $a_i(m,n)$; otherwise costs are $-\infty$. Notice that due the cyclic nature of graph, cost a_0 is also defined.

Fig. 4 schematizes the graph and the costs corresponding to the function $\Psi_n(\mathbf{r}^1)$. It is a layered graph (each layer corresponds to a scan-line), with connections only between pairs of nodes in successive layers. The starting and ending nodes (which are the same given the the cyclic topology of the problem) are chosen from scan-line $i = 0$.

Suppose, for a while, that we want to find the high cost path starting and ending at node $(0, n_0)$. This is a dynamic programming problem whose solution is given by Algorithm A0 (Bellman-Ford algorithm [41] tailored to the problem at hand). Therefore, Algorithm A0 provides the contour $\mathbf{r}^1$ that maximizes $\Psi_n(\mathbf{r}^1)$, constrained to $r_0^1 = d_0(n_0)$.

The high cost path, without any constraint, can be achieved by running the algorithm N_0 times, considering that in each run the solution path starts and ends at node $(0,k)$, with $k = 1, \ldots, N_0$. The greatest high cost path is the wanted solution. This approach increases the Bellman-Ford algorithm complexity by a factor of N_0.

recursive scheme provides, the high cost path between any node at any layer and node $(0, n_0)$:

Initialization: $i := 0$; $b_{0k} := -\infty$, $k = 0, \cdots, N_0$; $b_{0n_0} := 0$, $s := n_0$

For $i = 1, \cdots, M-1, 0$

For $k = 1, \cdots, N_i$

$$j_{max} := \arg \max_{j=1,\ldots,N_{i-1}} \big(a_i(j,k) + b_{i-1,j}\big)$$

$$b_{ik} := \big(a_i(j_{max}, k) + b_{i-1,j_{max}}\big)$$

$$n_{ik} := j_{max}$$

The solution $\mathbf{r}^1 = [r_0^1, \cdots, r_{M-1}^1]^T$ is given by:

(1) retrieve solution at node 0 (r_0^1):

$$r_0^1 := d_0(n_0)$$

$$s := n_{0s}$$

(2) retrieve solutions at nodes $i = M-1, \cdots, 1$ (r_i^1):

For $i = M-1, \cdots, 1$

$$r_{1_i} := d_i(s)$$

$$s := n_{is}$$

Instead of the previous approach, we adopt a suboptimal scheme which is based on the following informal argument: the solution components r_i^1 corresponding to scan-lines *far from* to scan-line $i = 0$ depend very little on the constraint $r_0^1 = d_0(n_0)$. Hence, we run Algorithm A0 twice: (1) in the first run the solution is constrained to be $r_0^1 = d_0(n_0)$, for a given n_0; (2) in the second run the component $r_{\lfloor M/2 \rfloor}^1$ (e.g., diagonally opposed to r_0^1) is constrained to be that obtained in (1). This scheme takes only 2 runs (instead of N_0) of Algorithm A_0. Although supported a different argument, the strategy just presented was proposed in [33] and therein named *two-loop* method.

For referencing purposes, we present below Algorithm A1 which implements the *two-loop* method. Notation $\mathbf{r}^1 := \text{Out}\big(\text{A0}[i, a]\big)$ means the solution contour $\mathbf{r}^1$ delivered by Algorithm A0 constrained to $r_i^1 = a$.

Algorithm A1: Implement the *two-loop* scheme.

$\mathbf{r}^1 := \text{Out}\big(\text{A0}[0, r_0^1]\big)$

$\mathbf{r}^1 := \text{Out}\big(\text{A0}[\lfloor M/2 \rfloor, r_{\lfloor M/2 \rfloor}^1]\big)$

Algorithm A1 searches for r_i^1 over its complete domain. This is not very efficient, since contour $\mathbf{r}^1$ lies in the neighborhood of $\mathbf{r}^1(n-1)$ with great probability. On the other hand, we know in

IMDP algorithm: Assume known $\widehat{\mathbf{r}}(n-1)$, to be given an integer m_0 specifying the coarsest resolution, an integer L specifying the number of searches per layer, and a real $\xi > 0$:

Initialize: $t := 0$, $\mathbf{r} = \widehat{\mathbf{r}}(n-1)$

For $t = 1, 2, \ldots,$

$\widehat{\mathbf{r}}(n) = \mathbf{r}$

Compute $\widehat{\boldsymbol{\sigma}}^t$ using (26), (27), and (28)

For $m = m_0, m_0 - 1, \cdots, 0$

$\mathbf{r}^1 := \mathrm{Out}\big(\mathrm{A1}[\mathbf{r}^1, m, L]\big)$

$\mathbf{r}^2 := \mathrm{Out}\big(\mathrm{A1}[\mathbf{r}^2, m, L]\big)$

If $\|\mathbf{r} - \widehat{\mathbf{r}}(n)\| > \xi$

continue loop t

Otherwise

$\widehat{\mathbf{r}}(n) = \mathbf{r}$

break loop t

advance that heart walls are surely larger than the intersample distance (in the present case the intersample distance is less than 0.3 mm). Thus, one can run algorithm A1 in a *multigrid* type fashion, firstly with a coarse resolution and covering completely the high probability zone, and next refining the estimate by searching in a smaller range, using a thinner resolution.

All the above ideas are implemented simply by constraining the search space to the set of nodes

$$\mathcal{N}[\mathbf{k}^1, m, L] \;=\; \Big\{(i,k) | k = k_i^1 + 2^m\, t, t = -L, \ldots, L, \;\; i = 0, \ldots, M-1\Big\} \cap \mathcal{N}, \qquad (31)$$

where $1 \leq k_i^1 \leq N_i$. Set $\mathcal{N}[\mathbf{k}^1, m, L]$ contains at most $(2L+1)$ nodes corresponding to each scan-line, centered at k_i^1 $\big(r_i^1 = d_i(k_i^1)\big)$ and 2^m apart. The maximum and the minimum attainable ranges are $\min\left[d_i(k_i^1 + 2^m L, d_i(N_i)\right]$ and $\max\left[1, d_i(k_i^1 - 2^m L)\right]$, respectively. Concerning Algorithm A1, 2^m denotes the coarseness of search, and $2L+1$ denotes the number of searches per layer.

Define $\mathbf{r}^1 := \mathrm{Out}\big(\mathrm{A1}[\mathbf{r}^1, m, L]\big)$ as the output $\mathbf{r}^1$ of algorithm A1 constrained to the set $\mathcal{N}[\mathbf{k}^1(\mathbf{r}^1), m, L]$. All the definitions and concepts supporting algorithm A1 concern the contour $\mathbf{r}^1$. They apply equally to contours $\mathbf{r}^2$, replacing index 1 by index 2, whenever necessary.

Algorithm IMDP, presented below, aims at the efficient determination of estimate $\widehat{\mathbf{r}}(n)$ given by criterion (23), using the iterative scheme (24)-(25).

We could have considered various iterations for each value of m. However, this proved not to be necessary, since for each t, the solution $\mathbf{r}$ provided by the inner **For** loop in the IMDP algorithm is, practically, the wanted one (the maximum of $\Psi(\mathbf{r})$ with respect to $\mathbf{r}$). This fact relies on the relatively high degree of independence (in the statistical sense) between $\mathbf{r}^1$ and $\mathbf{r}^2$.

(we are assuming that $N = N_0 = N_1 =, \ldots, = N_{M-1}$). Given a constrained search with $2L+1$ levels, $\Psi_n(\mathbf{r}^1)$ has to be computed $(2L+1)^2 \times M$ times. In the present work we adopt $L = 5$. For $N \simeq 150$ this means that the nonconstrained search demands a 185 times larger computational effort compared with the constrained search, what is quite a difference.

VI. Results

In all examples presented the number of scan-lines M is set to 32. We have chosen this number based on experimental results. Indeed, larger values of M would increase the computational effort (which is proportional to M), and would not lead to noticeable improvements on the contour estimates.

The IMDP algorithm was implemented on a NeXT DIMENSION workstation. It was parametrized with $L = 5$ and $m = 2$. These values will be kept along all experiments since they proved to be wise choices while leading to a mild amount of computation.

The stopping criterion of the IMDP algorithm depends on the parameter ξ. Instead of specifying it, the iteration is stopped when the estimated contours display no more visual changes. In all examples studied, this was accomplished with no more than 4 iterations ($t = 4$).

A. Simulated data

We first consider a set of simulated images of size 260×185. The pixel values are independent samples of a Rayleigh distribution. Pixel mean values were chosen according to the model presented in section III. Fig. 5(c) plots the estimated contours over the corresponding image. Reflectivities have values $\sigma_i^0 = 10$, $\sigma_i^1 = 30$, and $\sigma_i^2 = 100$ for all scan-lines. These contours were estimated from only one image. The starting estimate $\widehat{\boldsymbol{r}}(0)$, necessary to initialize the iterative algorithm (24)-(25), was obtained by maximizing the log-likelihood of each scan-line $L(I_i|\boldsymbol{r}_i, \sigma_i)$ with respect to $\boldsymbol{r}_i$ given by expression (8). Since vector $\boldsymbol{\sigma}_i$ is not *a priori* known, a crude estimate was computed: a Canny [18] type filter of width 20 was applied to the data along each scan-line. The inner contour position $\widehat{r}_i^1$ and the outer contour position $\widehat{r}_i^2$ were set to the positions corresponding to the two greatest maxima. Reflectivities $\widehat{\boldsymbol{\sigma}}_i^0$ were then computed according to (26), (27), and (28). In the sequel, the estimate $\widehat{\boldsymbol{r}}(0)$ will be called the ML estimate. Fig. 5(b) plots the ML estimate associated with data of Fig. 5(a) over each scan-line. Fig. 6 shows the estimated reflectivities associated to each scan-line of Fig. 5. Since the estimated contours exhibit almost no error, the variance of each $\widehat{\sigma}_i^k$ is only the one attributed to the sample power estimation.

The performance of the contour estimator depends only on the ratios σ_i^1/σ_i^0 and σ_i^2/σ_i^1 (see log-likelihood function (8)). The relative contrast of image in Fig. 5 is $\sigma_i^1/\sigma_i^0 \simeq \sigma_i^2/\sigma_i^1 \simeq 3$, for all

In order to have some insight on the trade-off between reflectivity contrast and estimation error, Fig. 7(a) considers a different pattern of reflectivity. It is generated with $\sigma_i^1/\sigma_i^0 = 2$ and $\sigma_i^2/\sigma_i^1 = 2$ for $i = 8, \cdots, 23$ and $\sigma_i^2/\sigma_i^1 = 0.5$ for $i = 24, \cdots, 7$. Thus, compared with the image of Fig. 5(a), there is not only a decrease in the relative contrast from 3 to 2, but also an inversion in the variation of reflectivity in the right side of the outer simulated tissue. This situation occurs frequently with real data. One can say that the estimated contour is a little worse than the one in Fig. 5(c). We have chosen a value of 2 (witch is equivalent to 0.5)[5] for the relative contrast σ_i^2/σ_i^1, since, with $\alpha_2 = \frac{5\times 10^2}{M^2}$, that value is the limit below which the outer contour becomes biased. Indeed, for $\sigma_i^2/\sigma_i^1 < 2$ the data does not produce enough *strength* to compete with the smoothness term. The net result is a biased outer contour estimate.

Concerning the inner contour, it is possible to have relative contrasts $\sigma_i^1/\sigma_i^0 < 2$ and still have acceptable estimates. Fig. 8 illustrate this situation. The relative contrasts σ_i^1/σ_i^0 and σ_i^2/σ_i^1 were set to 1.5. The outer estimate is biased, mainly near the points were the exterior ellipse shows the greatest curvature. The inner contour estimate is not as good as the one in Fig. 7(b). Roughly, one can say that it is a slightly smoothed version of the estimate plotted in Fig. 7(b). However, it is still good for many quantitative purposes.

The obvious conclusion of the example just presented is that the model parameters (in this case α_2) are not truly describing the data they were supposed to describe. For each example those parameters should be estimated. This is not, however, the perspective in which we place ourselves: we assume that parameters describing prior knowledge (α_1,α_2, and β_1) are constant, given the view from which data is acquired. This is also in accordance with the meaning of prior knowledge as the one not coming from the observed data.

B. Real data

The data set was obtained by a SIEMENS echocardiographic system, recorded on a video tape, and finally acquired with a NeXT DIMENSION video acquisition system. An ultrasound frequency of 2.5 MHz was used. A higher frequency would lead to higher contrast: the Rayleigh scattering (scatterers with linear dimensions D such that $D < \lambda/20$) is proportional to $\lambda^{-4}D^6$, [42]. Thus, by improving the acquisition process and using a higher frequency, a better data set could have been chosen. However, we use the present one in order to test the robustness of the proposed method.

Fig. 9(b) plots the ML solution over the frame 9(a) acquired at end-systole. The high contrast between myocardium and tissue outside heart on the southern hemisphere (inferior, posterior, and

[5] In fact, we have $\sigma_i^2/\sigma_i^1 = 2$ for $i = 8, \cdots, 23$ and $\sigma_i^2/\sigma_i^1 = 0.5$ for $i = 24, \cdots, 7$. However, concerning the contour estimator performance, contrasts c and $\frac{1}{c}$ are equivalents.

hemisphere (septum, anterior septum, and anterior wall) there is almost no contrast, this leading to a very poor quality ML estimate. The endocardial estimate, although not very far from the true endocardial contour, needs to be improved.

Figures 10 to 12 and 14 to 16 are subsets of a set with 25 frames to which the IMDP algorithm was applied (part (a) displays the original frame; part (b) overlays the estimated contours; part (c) overlays the hand traced contours). Actually, given the periodic heart movements, the algorithm was recursively and cyclicly applied: assuming an initial estimate $\widehat{\boldsymbol{r}}(0)$ (which can be, for example, the ML solution of frame 1) the estimates from 1 to 25 and from 25 to 10 are produced. Frames 1 to 10 are processed twice. The second time frame 1 is processed, the estimate $\widehat{\boldsymbol{r}}(25)$, instead of $\widehat{\boldsymbol{r}}(0)$, is used to initialize the algorithm. Thus, the undesirable impact of a rough estimate $\widehat{\boldsymbol{r}}(0)$ on the initial frames is removed. This scheme shares the spirit of the two-loop method proposed in [33].

Estimates plotted on Figures 11, 10, and 12 correspond to the end-systole frame, the previous one, and the next one, respectively. Estimates plotted in Figures 15, 14, and 16 correspond to the end-diastole frame, the previous one , and the next one, respectively.

Fig. 13 plots the estimated reflectivities $\widehat{\boldsymbol{\sigma}}_i$ of the image in Fig. 10(b). Blood reflectivity is systematically around $\widehat{\sigma}_i^0 \simeq 10$. Myocardium reflectivity is, in most of scan-lines, above 20, this leading to relative contrasts $\widehat{\sigma}_i^1/\widehat{\sigma}_i^0$ greater than 2. Reflectivity outside the heart has two different patterns: (a) in the northern hemisphere there is almost no contrast between myocardium and tissues outside the heart; (b) in the southern hemisphere, there is a high contrast between myocardium and tissue outside the heart. The poor contrast in the northern hemisphere leads to an estimate with greater variance. This is, in some degree, compensated by the higher smoothness of the outer contour. This can also be visually confirmed by comparing the automatic estimated contours 10(b), 11(b), 12(b) with the hand traced ones 10(c), 11(c), 12(c); the closeness between the hand traced and the automatic estimated contours is great even for the outer contour in northern hemisphere.

The remarks just presented concerning systolic frames shown in Figures 10, 11, and 12, apply equally to diastolic frames shown in Figures 14, 15, and 16.

Figures 14, 15, and 16 display the tips of mitral valve and/or the chordae tendinae near the papillary muscles, which is not considered in the model developed in this work. Nevertheless, we point out that the inner contour estimate was able to pass over these *artifacts*, whenever they are not touching the myocardium. This was made possible by implementing a preprocessing scheme for artifact detection and remotion. This procedure explores a simple fact: if a scan-line crosses an artifact inside the cavity and it is not touching the myocardium, then, the reflectivity profile exihibits a pulse-like pattern having the value σ^0 (blood reflectivity) in the lower level. Notice

reflectivity pattern, without artifacts, is always from a given value (blood reflectivity) to a higher value (myocardium reflectivity). Based on these arguments, the preprocessing scheme implements, for each scan-line, the following steps: (1) obtain a crude reflectivity estimate for each pixel; (2) for each pixel, compare, with hysteresis, the estimated reflectivity with the estimate of blood reflectivity; (3) if a path is marked as artifact, replace the correspondent pixels by the estimated blood reflectivity. Notice that the hysteresis referred in point (2) accommodates the estimate variance. This preprocessing scheme works reasonably well, given that artifacts and blood have very different reflectivities. This is evident concerning the artifact present in the neighborhood of the left papillary muscle, in Figures 14, 15, and 16.

Fig. 17 plots the evolution (from diastole to systole) of the quantity $\mathrm{Vol}\,\frac{3}{4c}$; symbol Vol stands for volume of left ventricle defined by epicardial and endocardial walls and c denotes the major hemiaxis (which can be determined from a long axis in the apical four-chamber echographic view). The volume was computed according to the ellipsoid model [5]. The concordance between the results using automatic contours estimation and manual contour tracing is evident.

The ejection fraction is given by the ratio between the stroke volume (difference between end-diastolic and end-systolic volumes) and the end diastolic volume. Assuming that the major hemiaxis c remains constant along the cardiac cycle, the ejection fraction is 0.70 when determined from the manual contours tracing and 0.68 when determined from automatic contours estimation. Again, there is a good agreement between automatic and manual based figures.

Finally, Fig. 18 plots the septum thickness evolution. Given the extremely poor contrast of echographic data in the septum and in its neighborhood, the results can be considered acceptable.

VII. Concluding Remarks

In this paper a method for endocardial and epicardial contour estimation in sequences of echocardiographic images is presented. The problem was formulated under the Bayesian setup. Contours are assumed two-dimensional, i.e. they have spatial and temporal indexes. For each temporal index, the contour is modelled as a noncausal first-order Markov random process. For each spatial index the resulting process is assumed as a causal first-order Markov random process. The physics of image generation and the heart morphology play a key role in building the image generation model; namely, the observed image pixels were modelled as Rayleigh distributed random variables with means depending on their positions relatively to the contours. The MAP criterion is then applied to derive the contour estimates. To solve the huge optimization problem one is led to, an algorithm embodying dynamic programming and multigrid aspects, which we named *iterative multigrid dynamic programming* (IMDP) was introduced. The IMDP algorithm

domain would have about 50 the IMDP complexity. The method is implemented and tested on a conventional workstation, and it takes less than 4 seconds to determine contours from a single image. Estimating the contours of a complete cardiac cycle takes, roughly, 1 minute.

Acknowledgment

The authors would like to express their gratitude to Dr. Seabra-Gomes and Dr. Canada from Instituto do Coração and Hospital de Santa Cruz for the precious cooperation and for providing the conditions that made this work possible.

References

[1] J. Dias and J. Leitão , "Wall position and thickness estimation from two-dimensional echocardiograms", *in IEEE Nuclear Science Symposium & Medical Imaging Conference*, pp. 1246–1250, S. Francisco, 1993.

[2] A. Weyman, *Cross-Sectional Echocardiography*, Lea and Febiger, Philadelphia, 1982.

[3] A. Buda and E. Delp, "Digital two-dimensional echocardiography", in A. Buda and E. Delp, editors, *Digital Cardiac Imaging*, pp. 41–60, Boston, 1985. Martinus Nijhoff.

[4] N. Shiller, "Echocardiography: Current status and future prospects", *Int. J. Cardiac Imaging*, vol. 1, pp. 41–60, 1985.

[5] T. Force, E. Folland, N. Aebischer, S. Sharma, and A. Parisi, *Echocardiographic Assessment of ventricular function*, chapter 19, pp. 374–401, W. B. Saunders Co., Philadelphia, 1991.

[6] L. Eaton, W. Maughan, A. Shoukas, and J. Weiss, "Accurate volume determination in the isolated ejecting canine left ventricle by two-dimensional echocardiography", *Circulation*, vol. 60, pp. 320–326, 1979.

[7] A. Macovski, *Medical Imaging Systems*, Prentice-Hall, 1983.

[8] S. Leavitt, B. Hunt, and H. Larsen, "A scan conversion algorithm for displaying ultrasound images", *Hewlett-Packard J.*, vol. 34, pp. 30–34, 1983.

[9] R. Snyder and J. Conrad, "Ultrasound image quality", *Hewlett-Packard J.*, vol. 34, pp. 34–39, 1983.

[10] D. Adam, H. Hareuveni, and S. Sideman, "Semiautomatic border tracking of cine echocardiogram ventricular images", *IEEE Trans. Med. Imaging*, vol. 6, pp. 266–271, 1987.

[11] P. Wallace, "Interpretation of the fluctuation echo from randomly distribuited scatterers. Part 2", *Candian Journal Physics*, vol. 31, pp. 995–1009, 1953.

aries by digital two-dimentional echocardiography", *IEEE Trans. Med. Imaging*, vol. 7, pp. 91–90, 1988.

[13] J. Kingler, C. Voughan, T. Fraker, and L. Andrews, "Segmentation of echocardiographic images using mathematical morphology", *IEEE Trans. Bio. Eng.*, vol. 35, pp. 925–934, 1988.

[14] N. Friedland and D. Adam, "Automatic ventricular boundary detection from sequencial ultrasound images using simmulated annealing", *IEEE Trans. Med. Imaging*, vol. 4, pp. 344–353, 1989.

[15] M. Unser, G. Pelle, P. Brun, and M. Eden, "Automated extraction of serial myocardial borders from M-mode echocardiograms", *IEEE Trans. Med. Imaging*, vol. 8, pp. 344–353, 1989.

[16] I. Herlin and N. Ayache, "Feature extraction and analysis methods for sequences of ultrasound images", *Image and vision computation*, vol. 10, pp. 673–682, 1992.

[17] E. Steen and B. Olstad, "Scale-space and boundary detection in ultrasound imaging, using signal-adaptive anisotropic diffusion", in Murray H. Loew, editor, *Medical Imaging 1994: Image Processing*. Proc. SPIE, 1994.

[18] J. Canny, "A computational approach to edge detection", *IEEE Trans. Pattern Anal. Machine Intell.*, vol. 8, pp. 679–698, 1986.

[19] F. Jeng and J. Woods, "Compound Gauss-Markov random fields for image estimation", *IEEE Trans. Signal Process.*, vol. 39, pp. 683–697, 1991.

[20] T. Simchony, R. Chellappa, and Z. Lichtenstein, "Graduated nonconvexity algorithm for image estimation using compound Gauss Markov field models", *in Proceedings of the International Conference on Acoustics Speech, and Signal Processing– ICASSP'89*, pp. 1417–1420, 1989.

[21] J. Zerubia and R. Chellappa, "Mean field approximation using compound Gauss-Markov random field for edge detection and image restoration", *in Proceedings of the International Conference on Acoustics Speech, and Signal Processing – ICASSP'90*, pp. 2193–2196, Albuquerque, 1990.

[22] M. Figueiredo and J. Leitão, "Adaptive discontinuity location in image restoration", *in Proceedings of the First IEEE International Conference on Image Processing – ICIP'94*, pp. II.665–II.669, Austin, 1994.

[23] P. Magnin, "Coherent speckle in ultrasound images", *Hewlett-Packard J.*, vol. 34, pp. 39–40, 1983.

[24] U. Montanari, "On the optimal detection of curves on noisy pictures", *Communications of the ACM*, vol. 14, pp. 335–345, 1971.

a dynamic programming searche algorithm", *Radiology*, vol. 155, pp. 513–517, 1985.

[26] A. Amini, T. Weymouth, and R. Jain, "Using dynamic programming for solving variational problems in vision", *IEEE Trans. Pattern Anal. Machine Intell.*, vol. 12, pp. 855–867, 1990.

[27] D. Geiger and A. Gupta, "Detecting and tracking the left and right heart ventricles via dynamic programming", in Murray H. Loew, editor, *Medical Imaging 1994: Image Processing*, pp. 391–402. Proc. SPIE, 1994.

[28] M. Figueiredo and J. Leitão, "A nonsmoothing approach to the estimation of vessel contours in angiograms", *IEEE Trans. Med. Imaging*, vol. 14, pp. 162–172, 1995.

[29] M. Figueiredo and J. Leitão, "Bayesian estimation of ventricular contours in angiographic images", *IEEE Trans. Med. Imaging*, vol. 11, pp. 416–429, 1992.

[30] E. Marcus, P. Lorente, E. Bartha, R. Beyar, D. Adam, and S. Sideman, "A comparative study of quantitative methods for characterization of left ventricular contraction", *in Proc. Computers in Cardiology*, pp. 145–148, Long Beach, 1985.

[31] P. Lilly, J. Jenkins, and P. Bourdillon, "Automatic contour definition on left ventriculograms by image evidence and a multiple template-based model", *IEEE Trans. Med. Imaging*, vol. 8, pp. 173–185, 1989.

[32] T. Pappas and J. Lim, "A new method for estimation of coronary artery dimensions in angiograms", *IEEE Trans. Acoust., Speech, Signal Process.*, vol. 36, pp. 1501–1513, 1988.

[33] D. Geiger, A. Gupta, L. Costa, and J. Vlontzos, "Dynamic programming for detecting tracking and matching deformable contours", *IEEE Trans. Pattern Anal. Machine Intell.*, To be published.

[34] S. Geman and D. Geman, "Stochastic relaxation, Gibbs distribution and the Bayesian restoration of images", *IEEE Trans. Pattern Anal. Machine Intell.*, vol. 6, pp. 721–741, 1984.

[35] J. Besag, "Spatial interaction and the statistical analysis of lattice systems", *Journal of the Royal Statistical Society B*, vol. 36, pp. 192–225, 1974.

[36] F. Lizzi *et al*, "Relationship of ultrasonic spectral pararametres to features of tissue microstructure", *IEEE Trans. Ultrasound. Ferroelect. and Freq. Contr.*, vol. 33, pp. 319–329, 1986.

[37] R. Wagner, M. Insana, and D. Brown, "Statistical properties of radio-frequency and envelope detected signals with applications to medical ultrasound", *J. Opt. Soc. Am.*, vol. 4, pp. 910–922, 1987.

[38] H. Karrer and A. Dickey, "Ultrasound imaging: An overview", *Hewlett-Packard J.*, vol. 34, pp. 3–6, 1983.

vol. 220, pp. 671–680, 1983.

[40] D. Bertsekas and J. Tsitsiklis, *Parallel and Distributed Computation. Numerical Methods*, Prentice Hall, New Jersey, 1989.

[41] R. Bellman, *Dynamic Programming*, Princeton University Press, 1957.

[42] A. Ishimaru, *Wave Propagation and Scattering in Random Media*, vol. 1, Academic Press, 1978.

1 Adopted polar coordinate system. 24
2 Echo along a radial scan-line from the heart center towards lung tissue. 25
3 Log-likelihood of the endocardial border. 26
4 Layered graph associated to the function $\Psi_n(\mathbf{r}^1)$. 27
5 Simulated image with $\sigma_i^1/\sigma_i^0 = 3$ and $\sigma_i^2/\sigma_i^1 = 3.33$ ($i = 0, \ldots, M-1$): (a) Original image; (b) ML solution $\widehat{\mathbf{r}}(0)$ associated with image (a) used to initialize IMDP algorithm; (c) Estimated contours. 28
6 Estimated reflectivities $\widehat{\sigma}_i^0$, $\widehat{\sigma}_i^1$, and $\widehat{\sigma}_i^2$ associated to each scan-line of Fig. 5(c), for $i = 0, \cdots, M-1$. 29
7 (a) Simulated image with $\sigma_i^1/\sigma_i^0 = 2$ and $\sigma_i^2/\sigma_i^1 = 2$ on the left hand size and $\sigma_i^2/\sigma_i^1 = 0.5$ on the right hand side; (b) Estimated contours. 30
8 (a) Image simulating faint data ($\sigma_i^1/\sigma_i^0 = \sigma_i^2/\sigma_i^1 = 1.5$ for all scan-lines); (b) Estimated contours. 31
9 (a) Frame at end-systole; (b) ML estimate. 32
10 Frame immediately before end-systole: (a) Original frame; (b) Original frame with automatic contours overlaid; (c) Original frame with hand traced contours overlaid. 33
11 End-systole frame: (a) Original frame; (b) Original frame with automatic contours overlaid; (c) Original frame with hand traced contours overlaid. 34
12 Frame immediately after end-systole: (a) Original frame; (b) Original frame with automatic contours overlaid; (c) Original frame with hand traced contours overlaid. 35
13 Estimated reflectivities $\widehat{\sigma}_i$ of image in Fig. 10(b) for $i = 0, \cdots, M-1$. 36
14 Frame immediately before end-diastole: (a) Original frame; (b) Original frame with automatic contours overlaid; (c) Original frame with hand traced contours overlaid. 37
15 End-diastole frame : (a) Original frame; (b) Original frame with automatic contours overlaid; (c) Original frame with hand traced contours overlaid. 38
16 Frame immediately after end-diastole: (a) Original frame; (b) Original frame with automatic contours overlaid; (c) Original frame with hand traced contours overlaid. 39
17 Estimated volumes defined by the endocardium and pericardium. 40
18 Estimated thickness of septum. 41

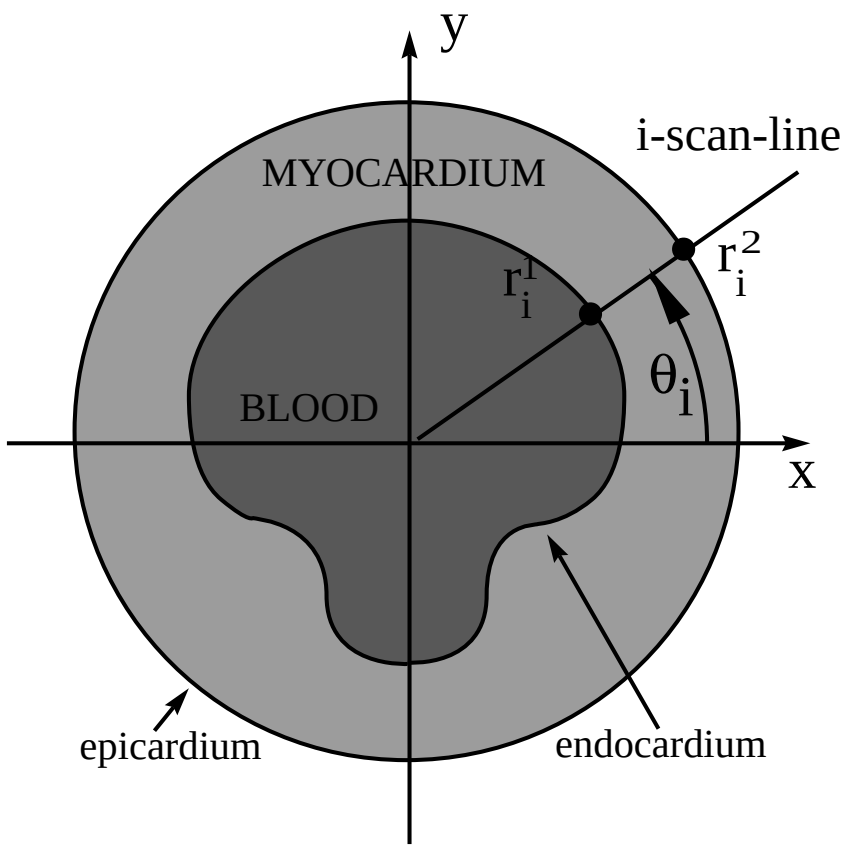

Figure 1: Adopted polar coordinate system.

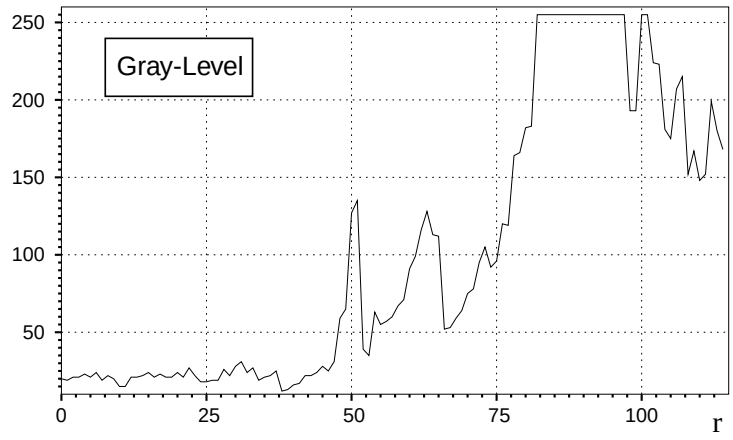

Figure 2: Echo along a radial scan-line from the heart center towards lung tissue.

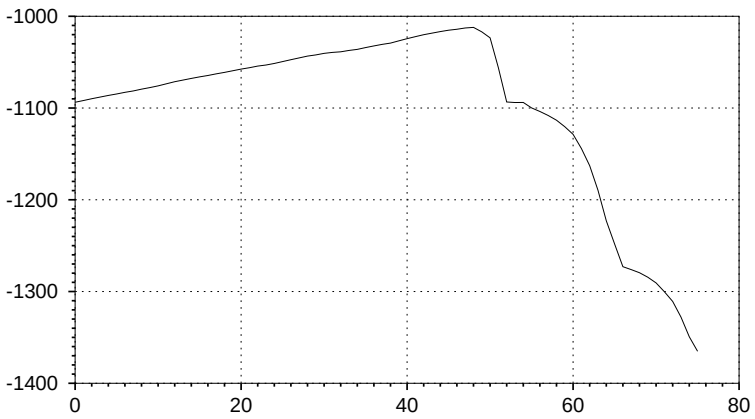

Figure 3: Log-likelihood of the endocardial border.

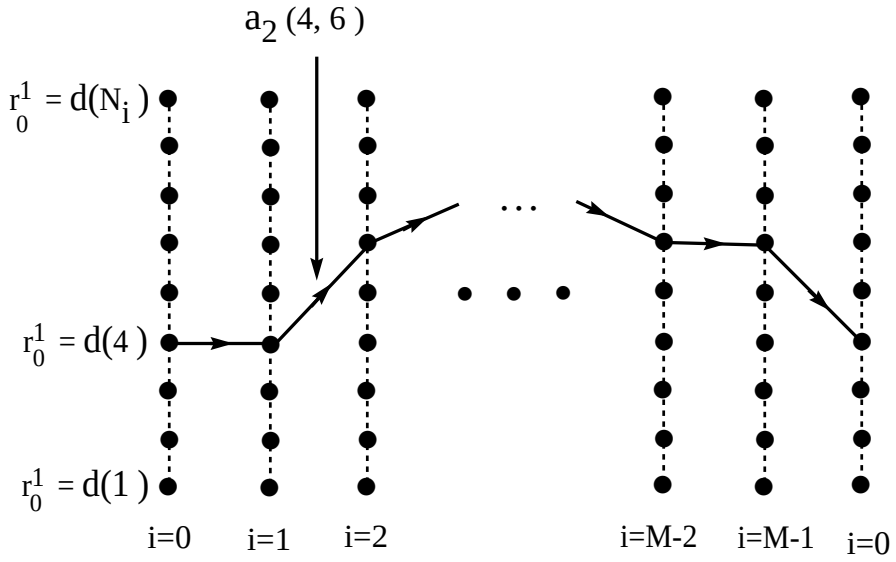

Figure 4: Layered graph associated to the function $\Psi_n(\mathbf{r}^1)$.

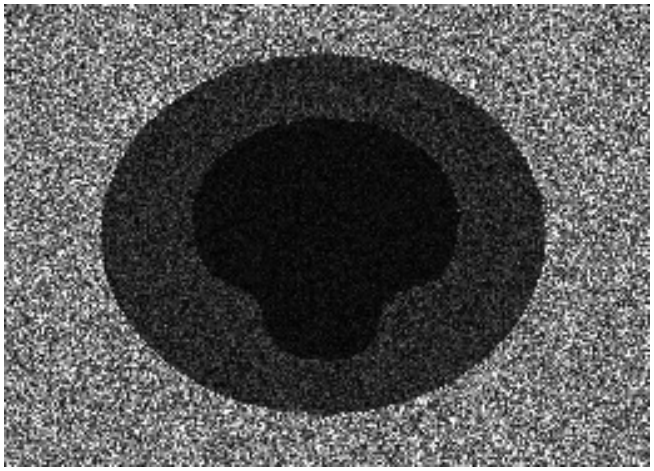

a)

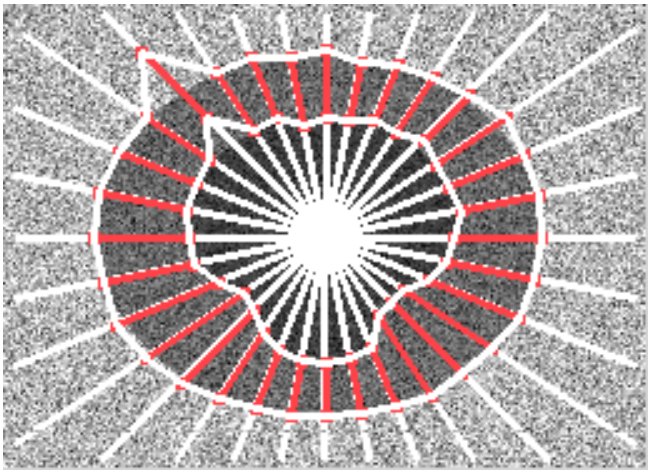

b)

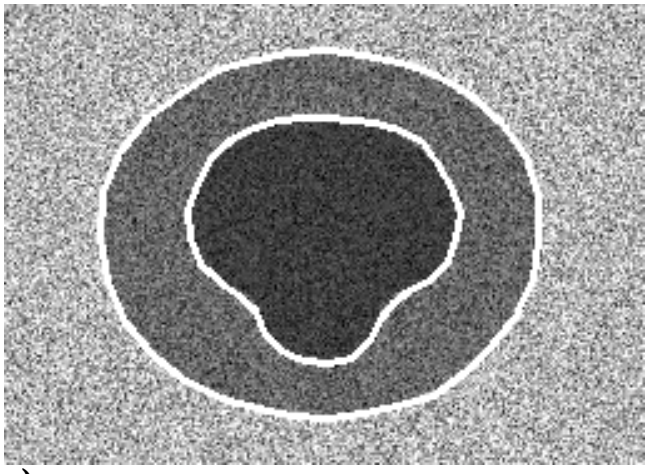

c)

Figure 5: Simulated image with $\sigma_i^1/\sigma_i^0 = 3$ and $\sigma_i^2/\sigma_i^1 = 3.33$ $(i = 0, \ldots, M-1)$: (a) Original image; (b) ML solution $\widehat{\mathbf{r}}(0)$ associated with image (a) used to initialize IMDP algorithm; (c) Estimated contours.

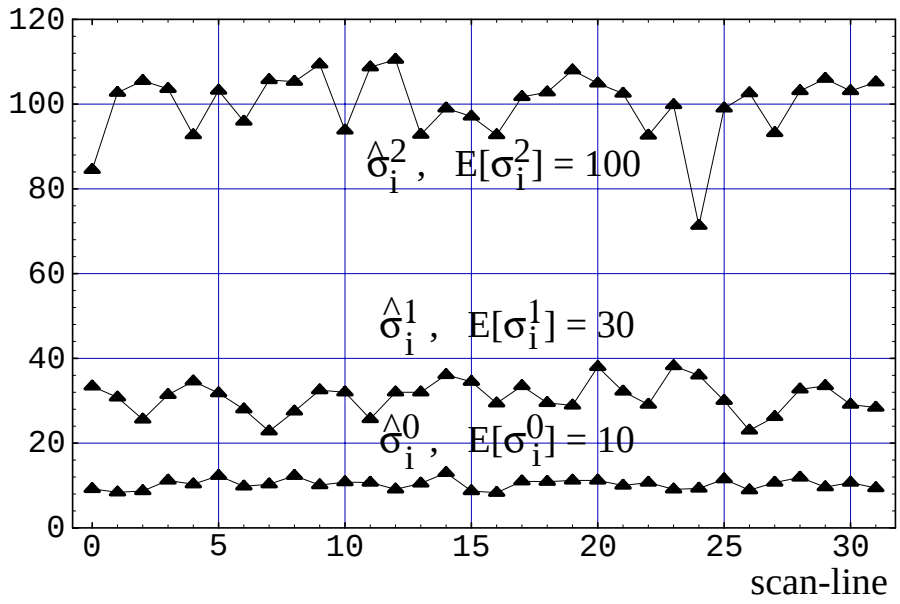

Figure 6: Estimated reflectivities $\widehat{\sigma}_i^0$, $\widehat{\sigma}_i^1$, and $\widehat{\sigma}_i^2$ associated to each scan-line of Fig. 5(c), for $i = 0, \cdots, M-1$.

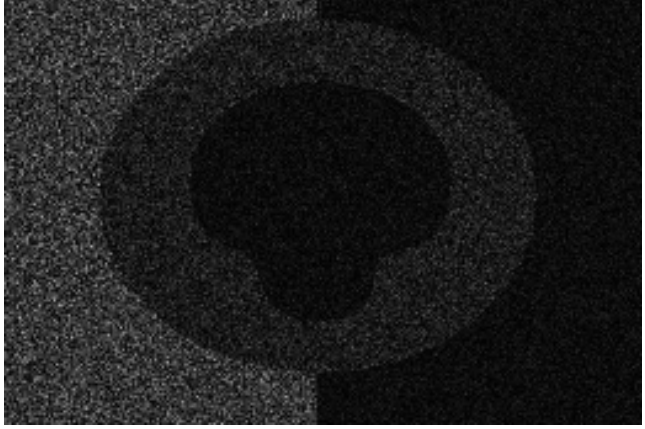

a)

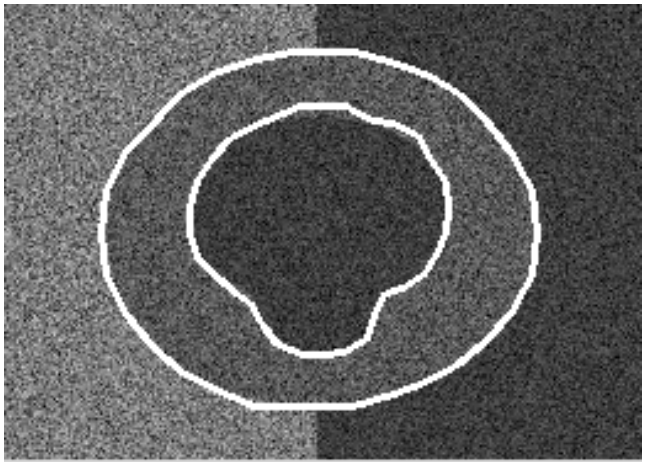

b)

Figure 7: (a) Simulated image with $\sigma_i^1/\sigma_i^0 = 2$ and $\sigma_i^2/\sigma_i^1 = 2$ on the left hand size and $\sigma_i^2/\sigma_i^1 = 0.5$ on the right hand side; (b) Estimated contours.

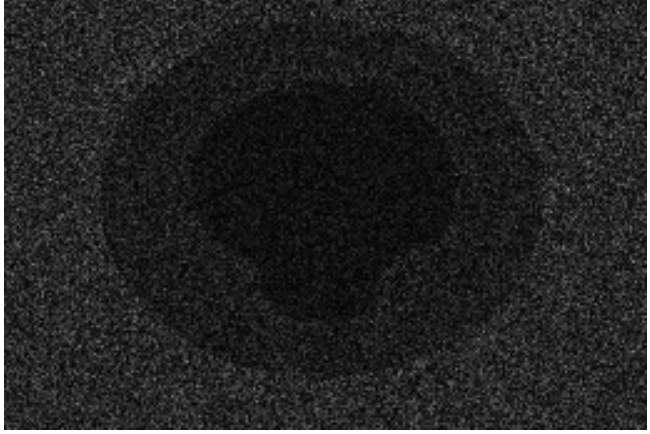

a)

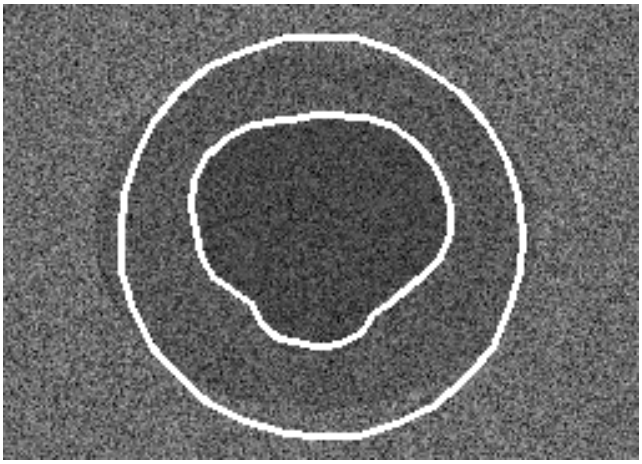

b)

Figure 8: (a) Image simulating faint data ($\sigma_i^1/\sigma_i^0 = \sigma_i^2/\sigma_i^1 = 1.5$ for all scan-lines); (b) Estimated contours.

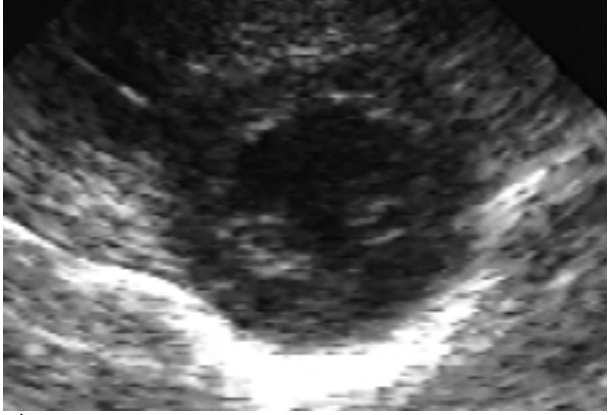

a)

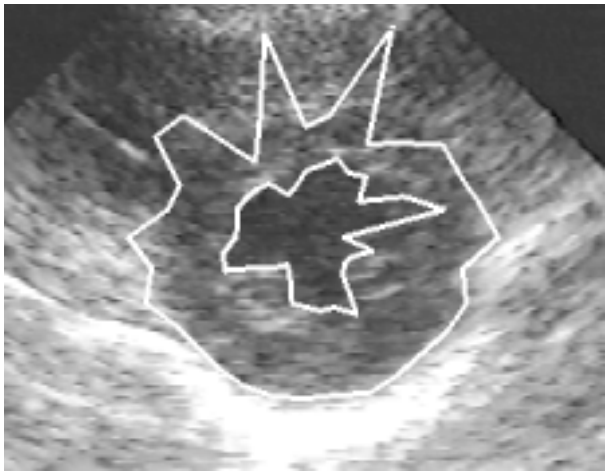

b)

Figure 9: (a) Frame at end-systole; (b) ML estimate.

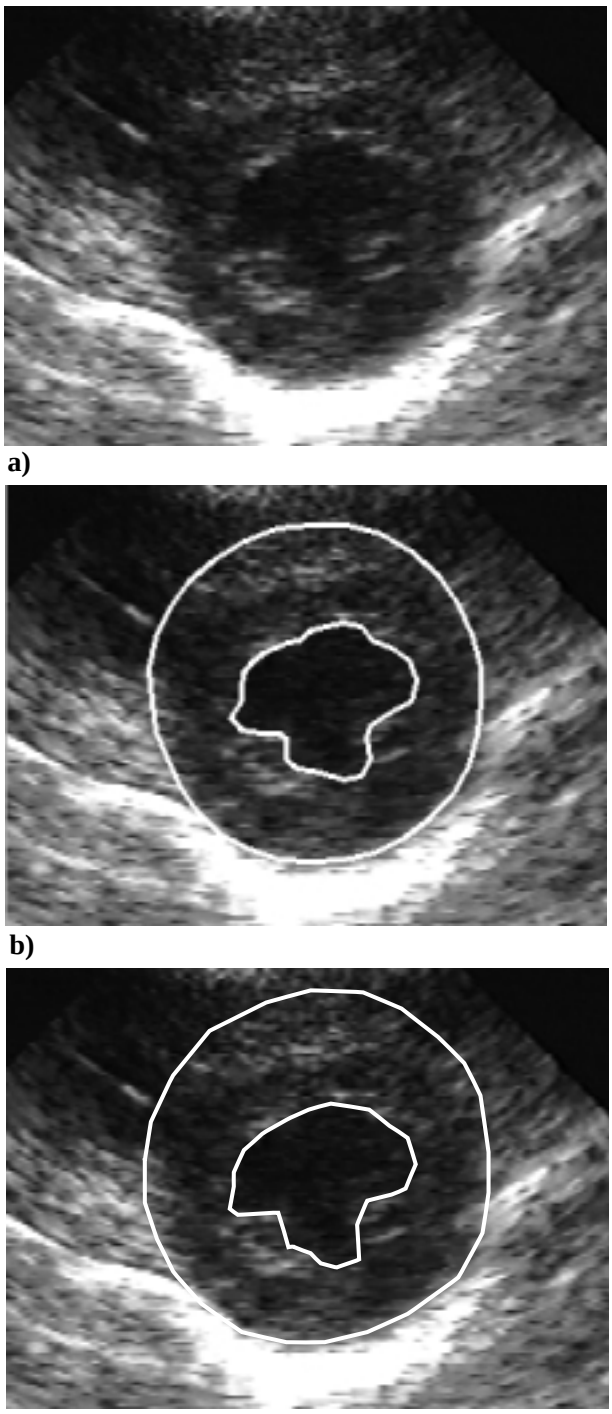

Figure 10: Frame immediately before end-systole: (a) Original frame; (b) Original frame with automatic contours overlaid; (c) Original frame with hand traced contours overlaid.

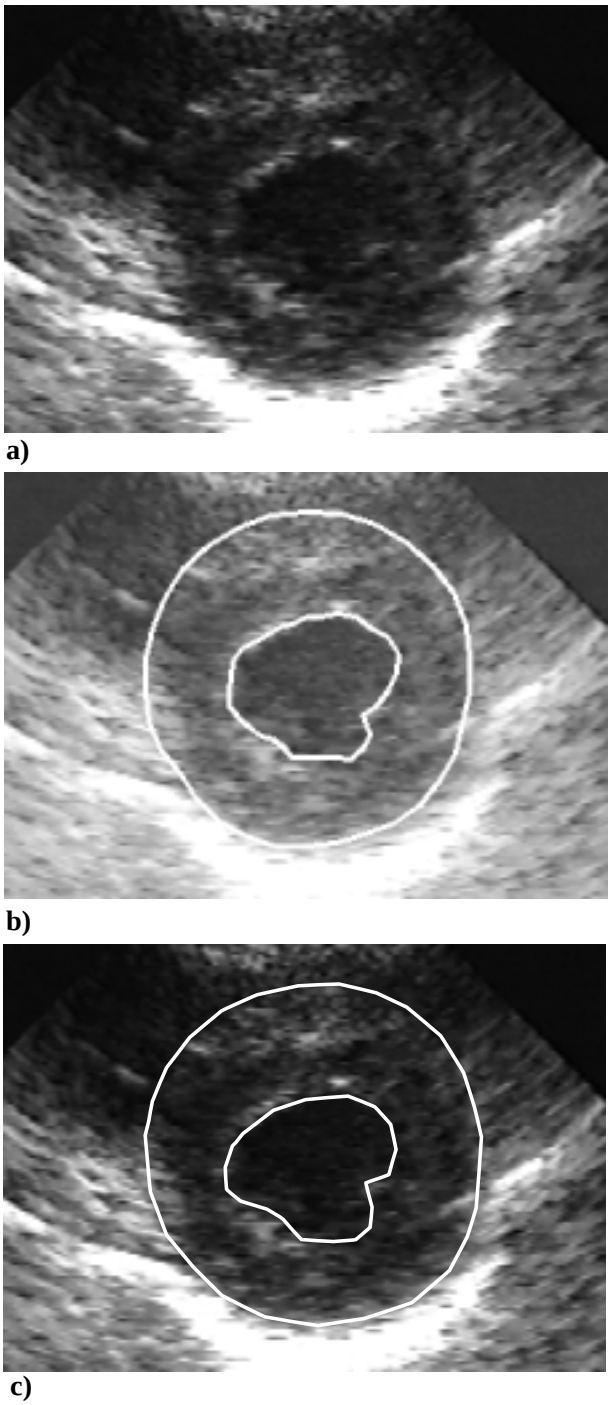

Figure 11: End-systole frame: (a) Original frame; (b) Original frame with automatic contours overlaid; (c) Original frame with hand traced contours overlaid.

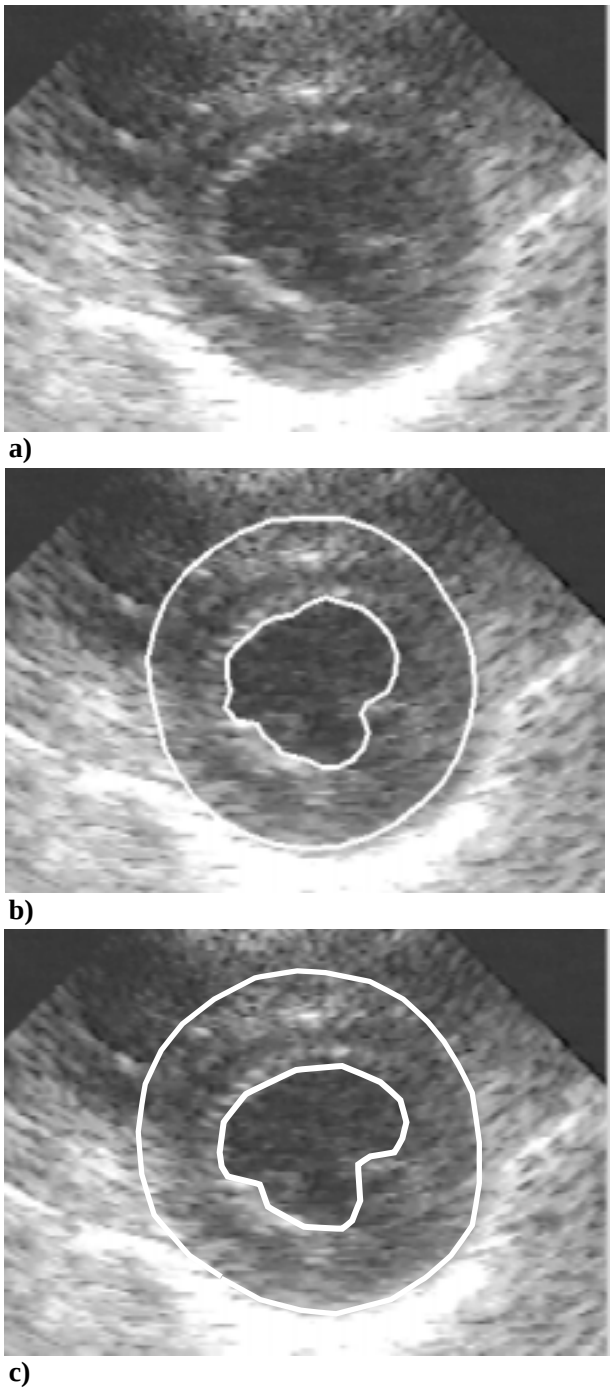

Figure 12: Frame immediately after end-systole: (a) Original frame; (b) Original frame with automatic contours overlaid; (c) Original frame with hand traced contours overlaid.

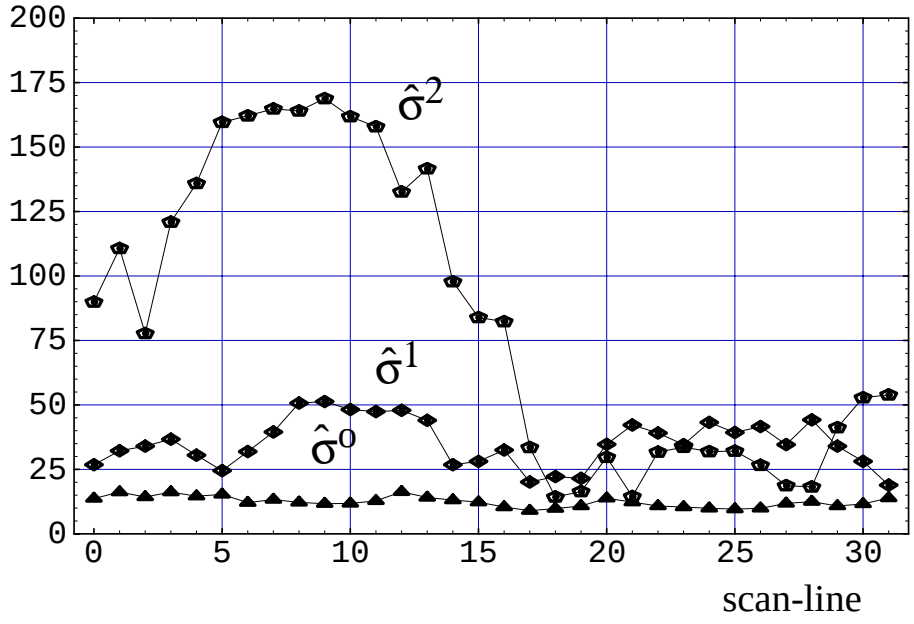

Figure 13: Estimated reflectivities $\widehat{\sigma}_i$ of image in Fig. 10(b) for $i = 0, \cdots, M-1$.

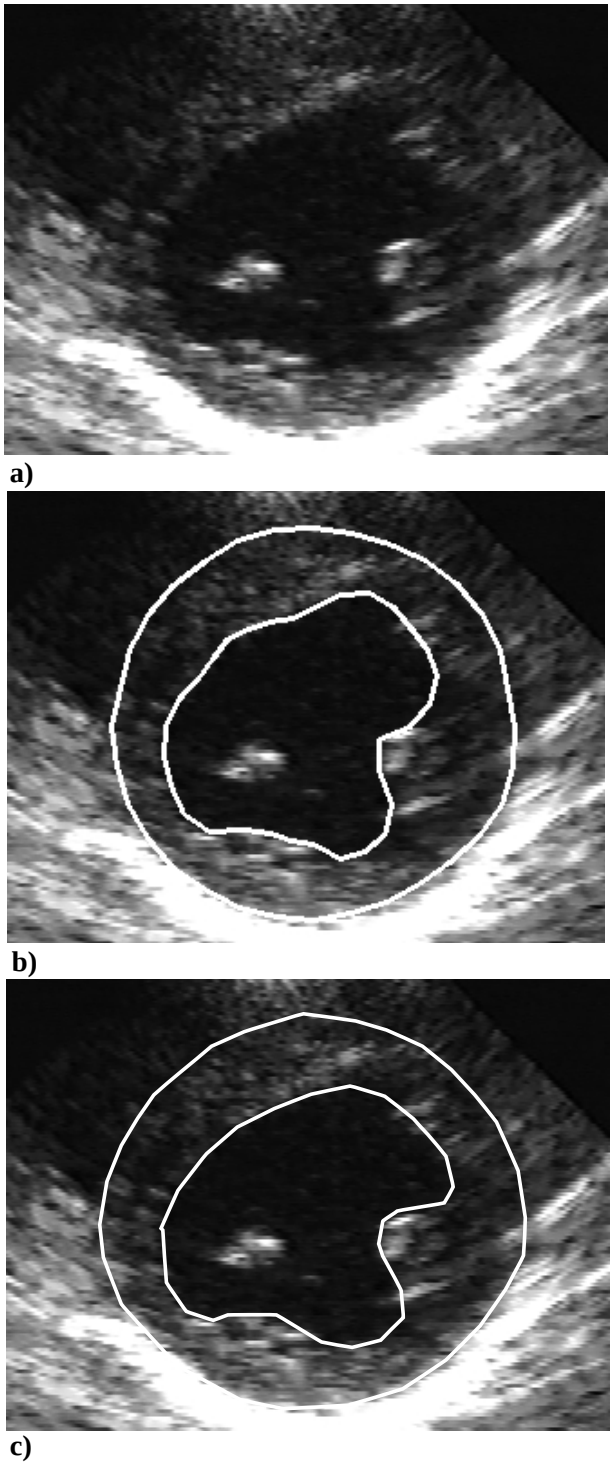

Figure 14: Frame immediately before end-diastole: (a) Original frame; (b) Original frame with automatic contours overlaid; (c) Original frame with hand traced contours overlaid.

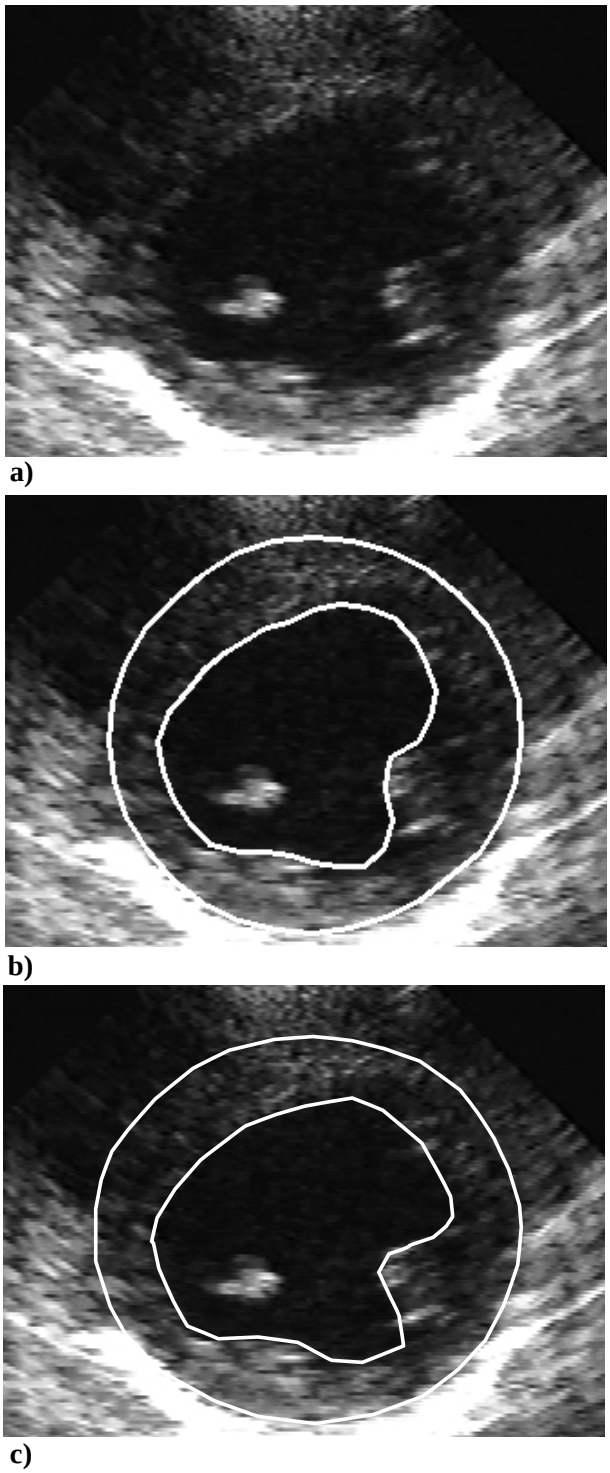

Figure 15: End-diastole frame : (a) Original frame; (b) Original frame with automatic contours overlaid; (c) Original frame with hand traced contours overlaid.

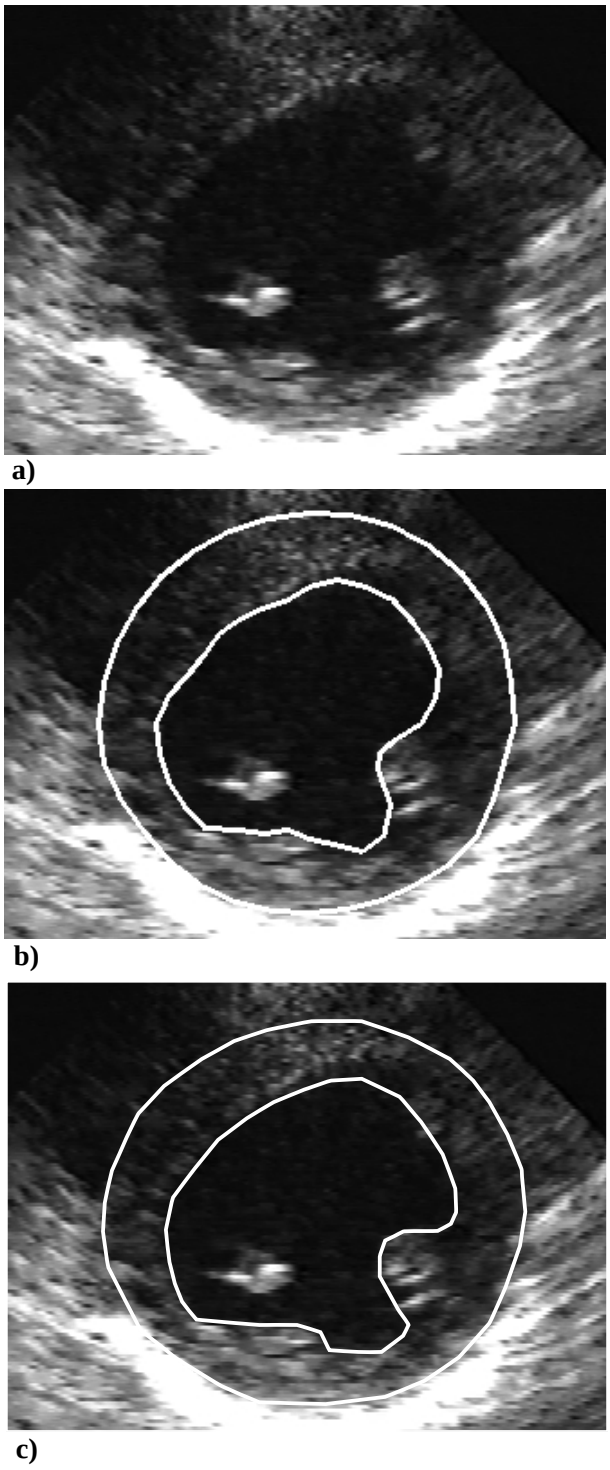

Figure 16: Frame immediately after end-diastole: (a) Original frame; (b) Original frame with automatic contours overlaid; (c) Original frame with hand traced contours overlaid.

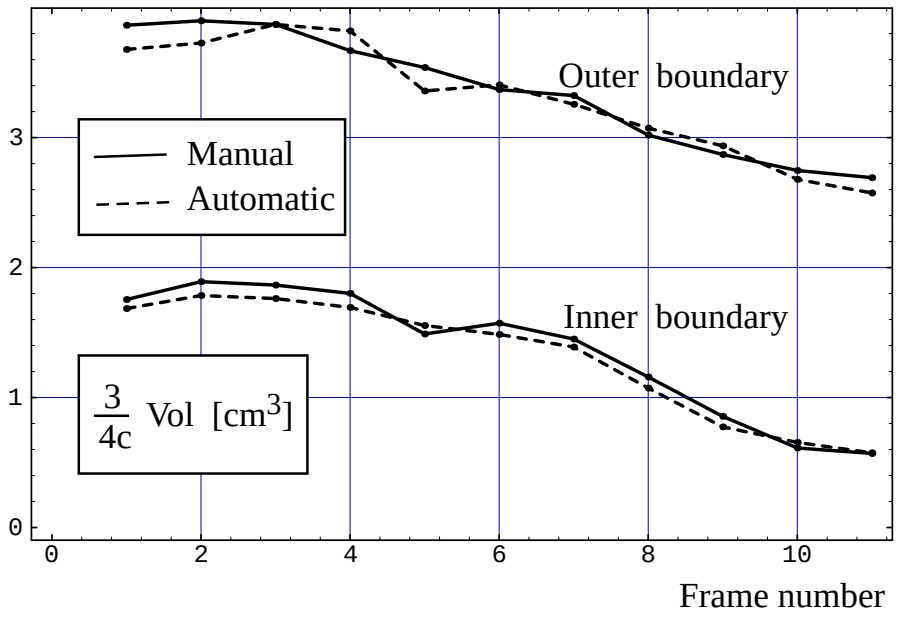

Figure 17: Estimated volumes defined by the endocardium and pericardium.

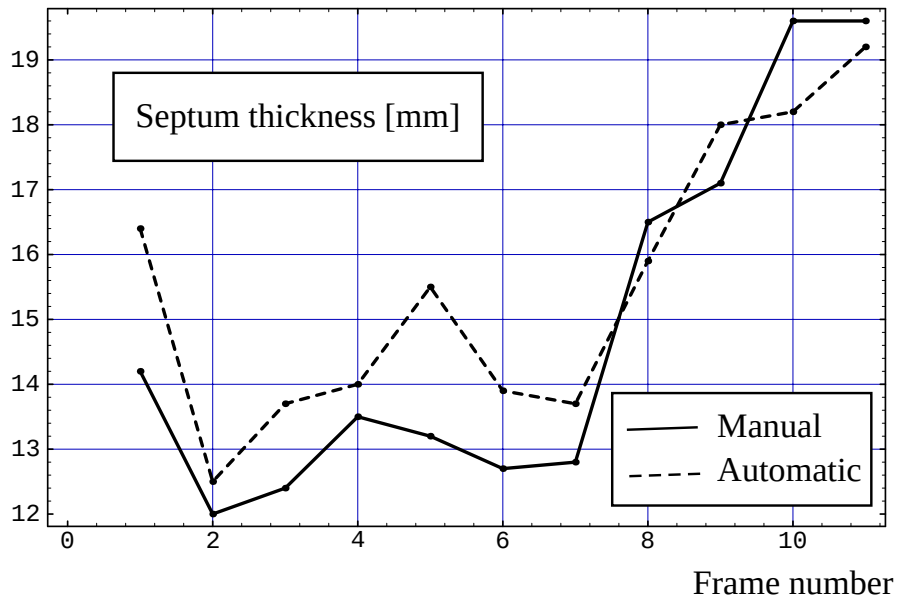

Figure 18: Estimated thickness of septum.